UNIVERSITY OF GHANA
COLLEGE OF BASIC AND APPLIED SCIENCES

COMPARISON OF METHODS OF μ-MAP GENERATION: MR-BASED METHOD IN PET/MR IMAGING VERSUS PSEUDO-CT METHOD IN RADIOTHERAPY DOSE PLANNING

BY

ISAAC KWESI ACQUAH

(10640003)

THIS THESIS IS SUBMITTED TO THE UNIVERSITY OF GHANA, LEGON, IN PARTIAL FULFILMENT OF THE REQUIREMENTS FOR THE AWARD OF MASTER OF PHILOSOPHY (MPHIL) MEDICAL PHYSICS DEGREE

DEPARTMENT OF MEDICAL PHYSICS

SCHOOL OF NUCLEAR AND ALLIED SCIENCES

JULY, 2019

DECLARATION

This thesis is the result of research work carried out by Isaac Kwesi Acquah in the Department of Medical Physics, School of Nuclear and Allied Sciences, University of Ghana, under the supervision of Dr. Stephen Inkoom, Dr. Francis Hasford and Prof Pal Erik Goa.

………………………… Date: ……………………

ISAAC KWESI ACQUAH

(STUDENT)

…………………………. Date: ……………………

DR. STEPHEN INKOOM

(PRINCIPAL SUPERVISOR)

…………………………... Date: ……………………

DR. FRANCIS HASFORD

(CO- SUPERVISOR)

…………………………… Date: ……………………

PROF. PĂL ERIK GOA

(CO-SUPERVISOR)

ABSTRACT

The main objective of this study was to compare the similarities and differences in MR-based and pseudo CT μ-map generation in PET/MR and radiotherapy respectively. The study sought to look at ways attenuation correction could be done on PET hybrid imaging systems and compare them in various ways so as to improve treatment and patient care. The methodology involved patient selection, image processing and generation of both μ-maps for PET-attenuation correction and pseudo CT for radiotherapy dose planning from computational software packages. MR-based μ-maps were successfully been generated and could be used to correct for attenuation in PET. Pseudo CTs were also successfully generated and could be used in radiotherapy for dose planning. For head images, it was observed that MR- based μ-maps over-estimated the bone as compared to CT μ-map for two patients, with deviations of 4.0% and 4.2%. Also, for head images, it was observed that the μ-values of bone for both MR-based and CT μ-maps were dynamic and had continuous values. For the pelvis, it was found that the pseudo-CT underestimated the bone volume as compared to CT μ-map in five patients, with deviations of 18.7%, 21.3%, 9.6%, 14% and 10%. It was observed that the μ-values of bone for pseudo-CT were not dynamic and also did not have continuous values as compared to CT μ-map. It was also observed from the pelvis studies that the μ-values for muscle were more dynamic and had a greater range in CT μ-map than the pseudo CT and MRI μ-map.

DEDICATION

This research is dedicated to my parents Very Rev Isaac Kwesi Acquah and Mrs. Paulina Acquah for their love, advice and the sacrifices they made to bring me this far. And to my entire family and friends for their support, prayers and encouragement, and finally to everyone who contributed to the success of this work.

ACKNOWLEDGEMENT

Glory and Honour to the Most High God for His everlasting kindness, grace, peace and love bestowed on me throughout this research.

I would like to express my utmost appreciation and gratitude to my supervisors; Dr. Stephen Inkoom, Dr. Francis Hasford, Prof. Pal Erik Goa and Prof. Live Einkens for their expertise in the field of research, exemplary guidance and extreme patience towards the research and the preparation of this thesis.

My sincere thanks also go to all the medical physicists and the staff at the radiotherapy and PET/MR center at St. Olav's Hospital- Norway for their assistance, suggestions and contributions towards this work.

I will also like to thank Dr. Gabriel Addio Nketiah and Prof. Kathrine Røe Redalen for their support and supervision towards the success of this work. I am very grateful.

I am also grateful to the coordinators of NORPART programme: Prof. J.J. Fletcher, Prof. Erik Păl Goa, Dr. Stephen Inkoom, Dr. Francis Hasford and Dr. Mercy Afadzi for the opportunity to undertake part of my research in Norway. Finally my sincere appreciation goes to all my lecturers and my colleagues at the School of Nuclear and Allied Sciences for their contributions in diverse ways.

TABLE OF CONTENTS

LIST OF TABLES

LIST OF FIGURES

LIST OF ABBREVIATIONS

AC	Attenuation Correction
CT	Computed Tomography
DICOM	Digital Imaging and Communication in Medicine
DRRs	Diagnostic Reconstructed Radiograph
FDG	Flourodeoxyglucose
FOV	Field of View
HU	Hounsfield Unit
ICRU	International Commission on Radiation Units and Measurement
LAC	Linear Attenuation Correction
LINAC	Linear Accelerator
MRI	Magnetic Resonance Imaging
NIFTI	Neuroimaging Informatics Technology Initiative
OAR	Organ at Risk
PET	Positron Emission Tomography
RT	Radiotherapy
ROI	Region of Interest
sCT	Synthetic Computed Tomography
SPM	Statistical Parametric Mapping
TE	Echo Time
TR	Repetition Time
UTE	Ultrashort Echo Time
ZTE	Zero Echo Time

CHAPTER ONE

INTRODUCTION

1.1 Background

Hybrid imaging system of positron emission tomography and magnetic resonance imaging (PET/MRI) is a modality which uses multi-parametric imaging technique to obtain morphological, functional and molecular information from the body. The system aligns the features of magnetic resonance imaging (MRI) such as soft tissue contrast, diffusion weighted imaging and dynamic contrast enhanced imaging with PET, providing quantitative physiologic and metabolic data (Cabello et al., 2015). The knowledge of photon attention coefficients of the various organs in the body is very useful in both PET imaging and radiotherapy (RT) dose planning in order to model correctly the attenuation and the dose distribution respectively (Commandeur et al., 2017). The established method for measuring photon attenuation coefficients has for a long time been by means of computed tomography (CT) (Dowling et al., 2015). However, with the introduction of PET/MRI as imaging modality, CT-based attenuation coefficient maps are no longer directly available, mostly in advanced countries (Edmund and Nyholm, 2017). Also, in radiotherapy the introduction of MRI as a replacement for CT in dose planning requires new methods for estimation of photon attenuation inside the body (Johansson et al., 2012).

There are different methods by which medical physicists specialized in PET/MR and those in RT go through to correct for attenuation. There are the segmentation or the bulk density override method, the atlas method and the voxel based methods which are discussed in detail in Chapter Two.

Figure 1 shows a PET/MR image acquired at the St. Olavs Hospital (Norway) and provides insight about the importance of attenuation correction in PET and how it helps to quantify an image properly for effective use. Attenuation correction has been one of the most important corrections of PET images, and as Figure 1 depicts, this correction is essential for both the visual appearance of the images and for the accuracy of quantifying radionuclide tracer uptake.

Figure 1.1: PET/MR image without attenuation correction (left) and with attenuation correction (right) (image courtesy of Anna Karlberg)

Attenuation is the progressive loss of energy by a beam as it traverses matter. A photon beam may be attenuated by coherent scattering, photoelectric effect, Compton scattering, pair production, triplet production or photodisintegration (Shandiz et al., 2017). For attenuation to happen, the beam must either be scattered or absorbed and this forms the basis of attenuation (Slates et al., 1999). In PET, attenuation is the loss of true coincidence events due to scattering or absorption of the annihilation photons before they both reach the detectors. The loss of detection of the photon due to attenuation increases image noise, image artifact and most importantly, the quantification of the image (Dowling et al., 2012). It is also important to note that attenuation increases as the body size increases (Fuchs et al., 2013). For the past years, attenuation in PET has been corrected by the use of low-dose CT images, since CT and PET were based on the same physical interaction. In Chapter Two of this thesis, a review is made of the ways in which attenuation is corrected in PET using MR images and also how to obtain attenuation information from MR images that would be used for treatment planning.

1.2 Objectives of this Study

1.2.1 Main Objective

The main objective of this study was to compare the similarities and differences between MR-based and pseudo-CT linear attenuation (μ) map generation in PET/MR imaging and radiotherapy respectively.

.

1.2.2 Specific Objectives

The specific objectives of this study were:

I. To generate μ-maps for both PET attenuation correction and pseudo-CT radiotherapy dose planning, using computational software packages

II. To compare the simulated pseudo CT for head and abdominal images.

1.3 Statement of the Problem

For several years, CT has been the choice of attenuation correction method in PET/CT hybrid imaging. However, due to limitations in soft tissue contrast posed by CT imaging, PET/MR has recently been a preferred choice for multi-modality imaging that focuses on soft tissues and fat. This is attributed to the superiority in tissue contrast on MR images than in CT images (Hofmann et al., 2008). PET/MR images provide detailed contrast and improved diagnostic value within tissues of diverse compositions. In both PET imaging and RT dose planning, it is important to know the photon attenuation coefficient inside the body in order to model correctly the attenuation and dose distribution respectively. For many years, this process has involved the acquisition of CT images which is based on the same physical interaction process, only at lower photon energies. The challenge has been limited to translating the Hounsfield unit (HU) values from the CT image to linear attenuation (μ) values at 511 keV for PET and to linear attenuation coefficient (μ) values for the photon spectrum of the linac. With the effort to replace CT with MRI in both PET imaging and RT dose planning, new challenges have emerged. Magnetic Resonance is based on a completely different type of physical interaction compared to CT, and there has not been any known relation between the MR signal and high energy photon attenuation coefficient (Carney et al., 2006). Instead, the chosen approach has involved MR-based tissue segmentation followed by assignment of pre-defined μ-values or HU values. This typically involves 4 tissue classes namely, soft tissue, fat, lung tissue and bone. Due to the organization of work in many hospitals across the world, PET/MR and MRI in RT most often do not involve the same people, and so there is little exchange of experience and knowledge between the physicists working on attenuation correction in PET/MR with those who work in applying MR-only RT dose planning.

1.4 Relevance and Justification of this Study

Much attention is being drawn towards MRI-only radiotherapy workflow since this improves patient care and treatment. This is because MRI gives us better soft tissue contrast, easy delineation of tumor and organ at risk, does not use radiation thereby optimizing dose to patient and many more. With all these advantages, there has been some setbacks towards the realization of these dreams (Puttick et al., 2015). One of the major setbacks is attenuation correction (Riola-Parada et al., 2016). MRI is based on a different physical interaction compared to CT. For successful dose planning in RT, there is the need for attenuation information. Hence, there is need to find ways to correct for this attenuation (Shandiz et al., 2017). This study sought to look at the many ways attenuation correction is done in the hospital and also to compare them in various ways so as to improve patient care and treatment.

1.5 Scope of Work

St. Olavs Hospital in Trondheim, Norway, received its first PET/MR in 2013 and the idea to implement MR in radiotherapy is in the process at the hospital. A lot of studies are therefore being done in the area of MR-based attenuation to support clinical implementation of such a new technology. In this study, a process of μ-map and pseudo-CT generation from two groups of physicists in the hospital (those in the PET/MRI and those in radiotherapy) were compared using various parameters. The study involved seven (7) patient images. Matlab software was used to write a computational algorithm for image processing, image registration, conversion from Hounsfield unit to PET linear attenuation coefficients, etc.

1.6 Organization of Thesis

This theses is arranged in chronological order of five chapters. Chapter one introduces the study of which comprises; the background of the study, objectives, problem statement, relevance and justification of the study and the scope of the work. Chapter two reviews existing literature relevant to the research problem. Chapter three focuses on the material and methodologies used for the study. Chapter four presents the results and the discussion performed. Chapter five is the conclusion of the study and recommendation made from this study.

CHAPTER TWO

LITERATURE REVIEW

2.1 Basic Photon Interaction

A photon is defined as a packet of energy. There are three possible outcomes that are bound to happen when X-ray or gamma ray interacts with matter. First scenario is where the radiation passes through matter without any interaction, second is the complete absorption of the radiation as it passes through matter, and last is the scattering of the radiation as it passes through matter (Wang et al., 2013).

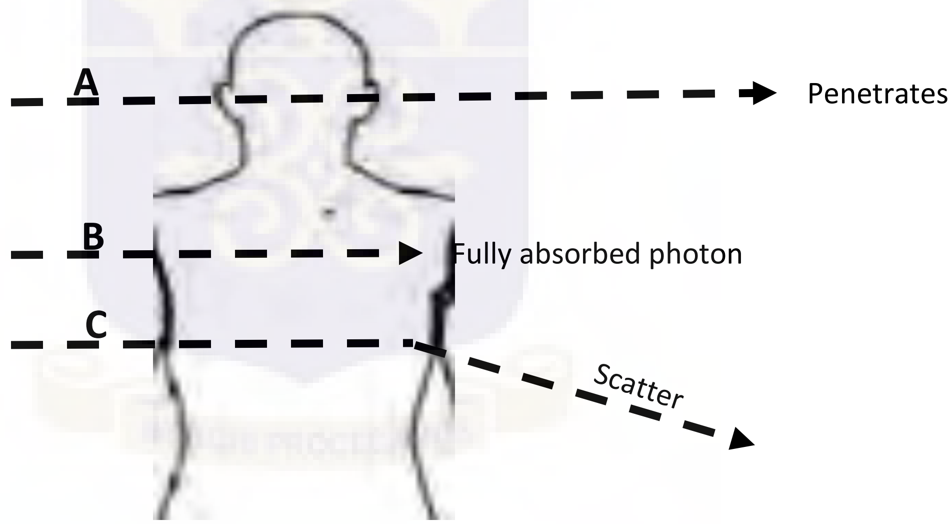

Figure 2.1: Illustration of the possible outcomes when a photon interacts with matter

As illustrated in figure 2.1, photon ‘A’ passes through matter without interaction, photon ‘B’ is absorbed completely by matter which leads to the photoelectric effect and for photon ‘C’ there is scattering of the photon by the body and this leads to Compton scattering. The interaction B and C form the basis of attenuation. In photoelectric effect, an electron is ejected from the inner shell by absorption of all the energy of a photon that interacts with it. When this happens an outer shell moves to fill the gap created and in doing so, emits X-ray radiation energy equal to the difference in binding energy between the two shells. For photoelectric absorption to occur, the incoming photon must have energies greater than the binding energy of the electron it interacts with. The probability of photoelectric effect decreases when the energy of the incident photon increases making it very predominant in lower energies like X-ray (70-1400 keV) than in higher energies like electron/positron annihilation (511 keV). The most important interaction in PET is Compton scattering. In this interaction, an incident photon interacts with the outer electron of an atom leaving the site of interaction in a different direction. The change in direction is termed scattering. The scattered photon leaves the site of interaction with lower energy as compared to the incident photon.

2.2 Positron Emission Tomography

Positron emission tomography (PET) is an important imaging modality which gives information of an organ at the molecular level. Despite this important information given by PET, the images produced are not well quantified due to loss of detection of true coincidence events at the detector as a result of attenuation, thereby resulting in a poor quantification and spatial resolution (Jung et al., 2016). To make up for this loss, scientists proposed the transmission technique for correcting attenuation and later proposed what is called attenuation correction through hybrid imaging modality, where two imaging modalities are put together. The idea of PET/MRI dates back to the early 1990s even earlier than the advent of PET/CT, but the challenges associated with this modality hindered its realization (Christensen et al., 1995). The first hybrid modality that was established in the clinical field was the PET/CT in the University of Pittsburgh Medical Center in 1998, where a low resolution CT image was taken to generate a μ-map to correct for the low photon intensity areas in the PET image thereby correcting for attenuation (Keereman et al., 2013). At the same time, scientists were working on other hybrid imaging modalities. Although the images produced by PET/CT were better, other information that were relevant for diagnosis and therapy were lacking. Combining PET and MRI seems to be the ideal hybrid imaging modality since that would give better information for diagnosis and radiotherapy and these came with lots of challenges.

2.3 Importance of PET/MRI

Magnetic Resonance Imaging gives excellent anatomical information with enhanced contrast with soft tissue while PET provides additional functional information about the internal organs at the molecular level making this hybrid modality an excellent choice (Glide-Hurst et al., 2014). MRI does not use ionizing radiation so it allows for multiple scans without any concern of patient exposure to ionizing radiation. MRI gives the luxury to scan with different sequences which helps to improve image quality (Karlsson et al., 2009).

2.4 Challenges of PET/MRI

Unlike PET/CT, the realization of this excellent hybrid imaging modality has been hit with lots of challenges. This started with the interference of the magnetic field with the PET detector system (Slates et al., 1999) which now has been solved with the advent of semiconductor detectors. Also the other problem was how to place these two machines together to reduce scan time. Another problem faced in PET/MRI was attenuation correction in the PET with MR images. Also another hurdle was the PET component interfering with the radio frequency (RF) of the MRI machine which lead to the production of eddy currents around the conductive part of the PET resulting in the generation of heat (Peng et al., 2010; Pichler et al., 2008). A lot of research has currently led to the use of carbon fibre as shielding materials for the conductive component of PET and has proven to be very successful (Peng et al., 2014).

2.5 Attenuation

Attenuation with respect to PET is the loss of detection of true coincidence events from reaching the detector level due to the absorption or scattering (attenuation) by the internal organs of the body. This loss in the intensity in PET imaging due to the absorption or scattering can range from 50-90% and increases as the size of the body increases (Jung et al., 2016). This attenuation in the body when imaging leads to poor images produced by PET, therefore, to obtain highly quantified, well resolved images with high spatial resolution, attenuation correction needs to be done. The major challenge of correcting this attenuation is finding good attenuation correction factors to make up for this loss. Figure 3 illustrates how true coincidence is lost due to absorption as indicated in diagram B and also scattering as indicted in diagram C. For diagram A, it is observed that when no patient is placed in the PET scanner, there was a true coincidence detection, unlike that illustrated in diagram B and C where there is loss of true coincidence due to absorption and scattering respectively.

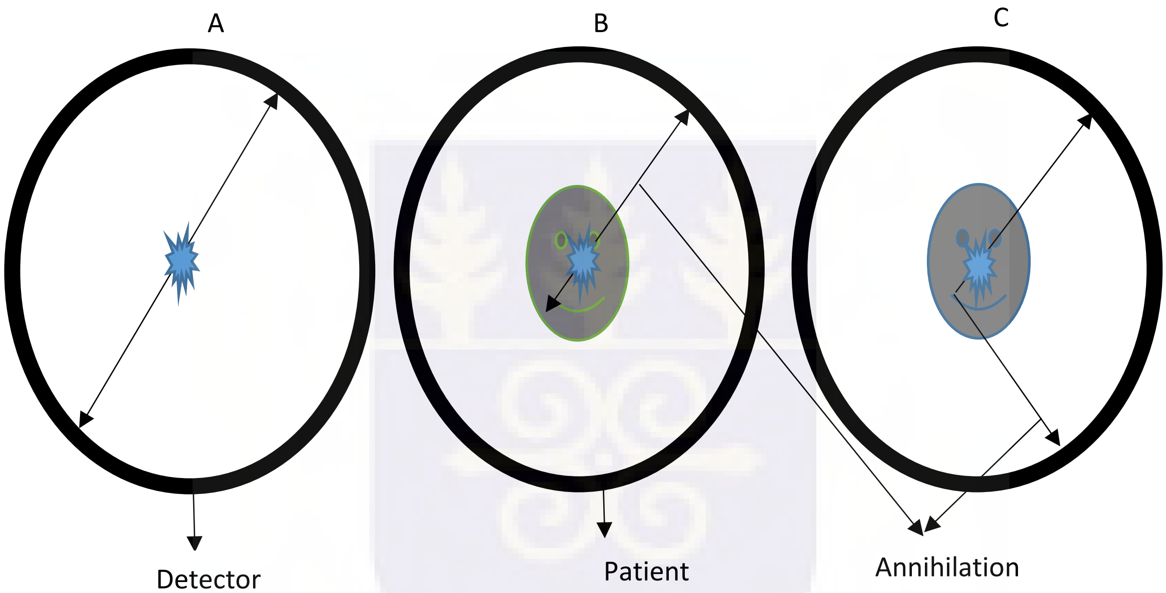

Figure 2.2. Annihilation process in PET without patient (A) and within patient (B and C) Respectively.

2.6 Attenuation Correction

Before the use of CT or MRI for attenuation correction in PET, the process used was the transmission technique. In this method, a radioactive source (mostly ceasium) is placed at one side and a detector placed on the opposite side, the source is moved 360° around the body and the radioactivity in the detector is measured as a function of the angle. The process is then repeated again, this time with no body in the gantry as illustrated in figure 2.3. Caesium is used because it has energy of 662 keV and since attenuation is measured at 511 keV, it gives a very good approximation. Comparison is made between the two and attenuation is corrected.

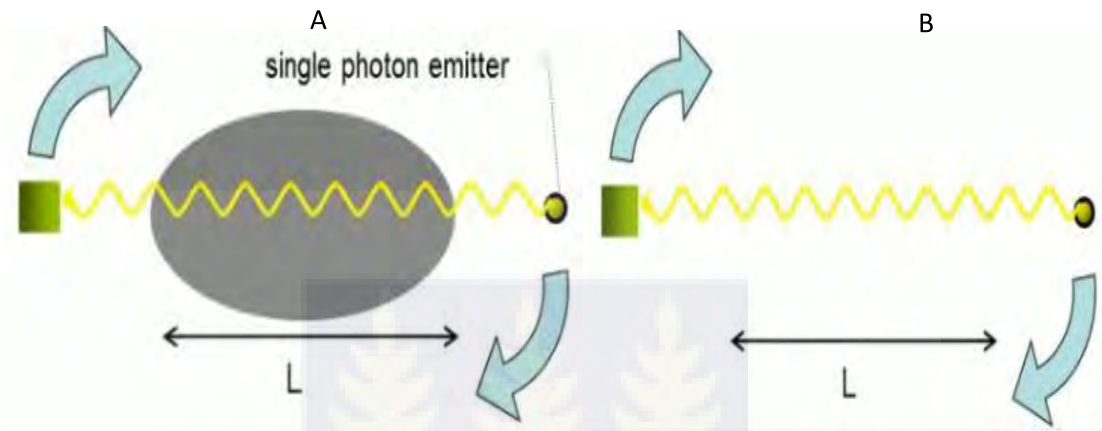

Figure 2.3: Transmission technique attenuation correction showing measurement with patient (A) in the gantry and without (B) patient in the gantry.

For the past years, correcting for loss in photon energy has involved the acquisition of CT images which undergo the same physical interaction as PET only at lower photon energies. The CT image gives information about the attenuation coefficient and for that matter the electron distribution in the body, very useful information in PET attenuation correction and also radiotherapy treatment planning (Sjolund et al., 2015). This information helps to know the dose distribution in the body when planning for treatment in cancer patients, making CT the easiest modality to combine with PET.

In recent years, with the introduction of PET/MRI in clinical care, scientists are finding several ways to correct for attenuation. Unlike CT which undergoes the same physical interaction as in PET, MR images are based on different physical interaction. Image formation in MRI is based on hydrogen (proton) distribution in the body for imaging, making it difficult to correct for attenuation. Figure 2.4 illustrates images acquired by the physics team at the PET Center in St. Olavs Hospital in Trondheim showing a phantom image before and after attenuation correction. It is observed that the images are well quantified in the second (right) one with high spatial resolution.

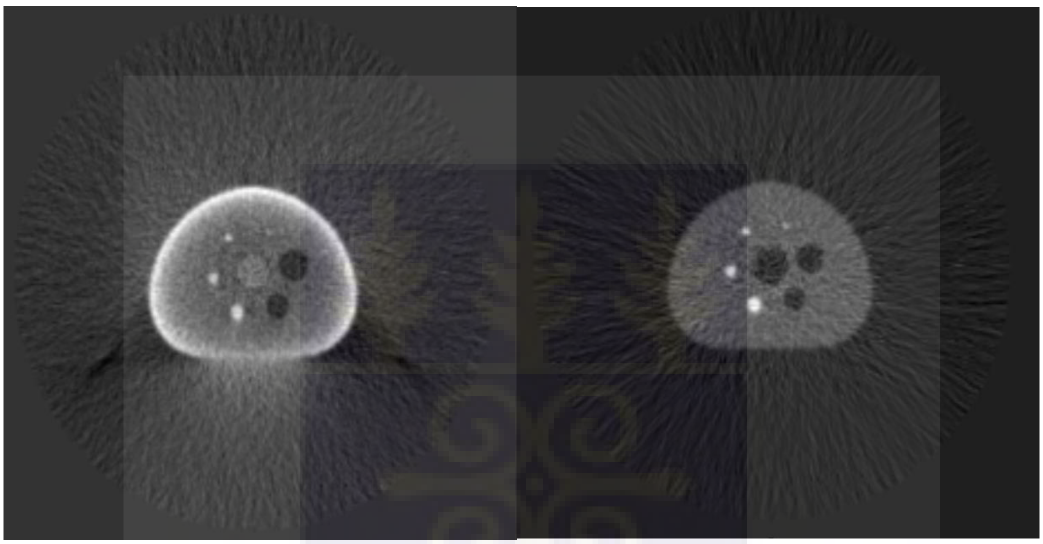

Figure 2.4: Phantom image taken on PET system illustrating attenuation correction (Courtesy of Anna Karlberg).

With PET becoming very useful in the clinical field, scientists have found different ways of correcting for this attenuation using MR images. Some of the various methods currently in use are discussed below:

2.6.1 Segmentation-Based Approach

This method of correcting for attenuation is one of the earliest and most common method used in correcting for attenuation in PET. After the acquisition of the images from PET and MRI, the two images are co-registered and the resulting image is then segmented into a fixed number of tissue classes, and a predefined μ-value or HU is assigned to them. The earlier approach involved only three classes (air, lung, and soft tissue) or four if fat is considered. Bone is neglected since it is not visible in T_1-weighted or Dixon MR Images, leading to a significant quantification error in the body part where bone was dominant (such as head, pelvis, etc.). This is because in the T_1-weighted and Dixon MR images both air and bone have similar MR signals but different attenuation effects (Chen and An, 2017) because bone has higher density. Due to the shortfalls in the earlier approach, different imaging sequences have been developed in MR imaging where air, lungs, soft tissue and bone are present in order to improve the attenuation correction map. Most of these incorporate the ultrashort echo time (UTE) and zero echo time (ZTE) MRI techniques (Jung et al., 2016).

Zaidi et al 2003 were one of the early scientists to work on attenuation correction on PET. Their method was the segmentation method where a T_1-weighted image from MRI was realigned to preliminary reconstruction of PET data using an automated algorithm and then segmented by means of a fuzzy clustering technique which identified tissue of significantly different density and composition. The voxels belonging to different regions were classified into air, skull, brain tissue and nasal sinuses. The attenuation coefficient values were assigned based on the recommendation of white et al. (2016). In conclusion a small improvement in the image produced was obtained and their study broadened the knowledge of the segmentation method across the world alerting other scientists to improve upon it (Zaidi et al., 2003).

Paulus et al (2015) also worked on this novel approach of attenuation correction where bone was included in the tissue classes. In this method, the Dixon sequence was used to acquire the MR-images and bone information was added using the model-based bone segmentation algorithm. This segmentation algorithm is made up of a set of aligned MRI data and bone masked pair for each major body bone individually. As a control experiment, CT-based μ-maps were also generated using the PET/CT data from the patients. A significant improvement in the images from the PET especially in the bony tissues and nearby soft tissues was obtained (Paulus et al., 2015).

2.6.2 Atlas Registration Approach

The atlas or template registration approach also is a direct imaging method with segmentation and continuous linear attenuation correction (LAC) value conversion. This is a method used to predict the attenuation coefficient on a continuous scale. In this method, the MR-images of a PET/MRI examination are co-registered to a template or a number of atlases. The resultant image is used to generate a patient specific attenuation map. In the work by Cabello et al (2015) on MR-based attenuation correction in dementia patients using ultrashort-echo time pulse sequence, the researchers incorporated the global based thresholding method to generate the air mask. In the extraction of bone tissue, R_2 computations were made to generate a μ-map to separate bone from air. R_2 is the inverse of the spin-spin transverse relaxation time from which the mu-map was derived. The CT images were co-registered with MR-images in the way that the bone voxels were linearly equalized to the corresponding CT signal intensity and then the linear attenuation values in the bone were generated using R_2 scale. This method was compared with the μ -maps calculated from the MR-scanner, the μ -MAP_{DX} and the μ -MAP_{UTE}. The result was that the R_2-based map gave more accurate quantitative information than the rest (Cabello et al., 2015).

2.7 Role of PET/MRI in Radiotherapy Treatment Planning

In recent years, various efforts have been placed in the radiotherapy field to improve the quality of treatment. Radiotherapy has moved from the use of cobalt 60 machine to linear accelerator where highly modernized techniques like intensity modulated radiotherapy (IMRT), volumetric modulated radiotherapy (VMAT), proton therapy (PT),etc. are being used to improve the quality of treatment. These advanced radiotherapy techniques can spare a lot of healthy organ tissues whiles tumor or cancerous cells would be effectively damaged. With the advent of PET/MRI in the clinical field, the information given by this hybrid system in terms of the excellent anatomical and functional information would help in accurate diagnoses and treatment planning. MRI does not use ionizing radiation, thus reducing the patient exposure and has the ability to scan multiple times using different imaging techniques; as a result, different patho-physiological measurement such as vascularization, perfusion, metabolism and hypoxia can be visualized simultaneously (Thorwarth et al., 2013).

2.8 Pseudo CT Generation

Generally, treatment planning in the radiotherapy setting has solely depended on CT images. However, with the advent of MRI and MRI-linac and their integration into the clinical field, most studies in recent focus on MRI-only workflow for radiotherapy treatment planning. This is due to reduction in patient dose, excellent soft tissue contrast, higher delineation in target and organ at risk (OAR) and simplified pathway for patients towards treatment (Wang et al., 2013). The major setback hindering the realization of these dream is that MRI does not give electron density information which is needed for radiotherapy dose calculation (Wagenknecht et al., 2013). This is because MRI is based on a different physical interaction. Unlike CT, MRI signal intensity does not have a direct relationship with electron density. Instead, it depends largely on proton density and tissue relaxation properties (Karlsson et al., 2009). This setback makes it very difficult to use MRI directly in radiotherapy treatment planning necessitating the need to find a way to correct for electron density; this led to the introduction of pseudo-CT (also called synthetic CT, substitute CT) which is an MR-image with electron density information. There are three major ways through which pseudo-CT could be generated according to literature (Edmund and Nyholm, 2017). The three ways are bulk density override techniques, atlas base-technique and voxel-based technique.

2.8.1 Bulk Density Override

Assigning bulk density to the volume in patient is recognized as one of the easiest methods of correcting for attenuation in an MR image. In this method, it is assumed that a volume in the body is homogenous and then attenuation values are assigned for the dose calculation. Another way is to put the various tissues in the MRI into different classes (soft tissue, bone and sometimes air) and then assign electron density values to them. Ramsey and olive (1998) were among the earliest scientists to report on pseudo-CT generation

(Ramsey and Oliver, 1998). In their work, they used an anthropomorphic Rando head phantom to obtain a T_1-weighted image using a 1.5 T MRI unit, corresponding CT images were also taken. Diagnostic reconstructed radiographs (DRRs) were generated using MRI and CT images. It emerged that the MR-based DRRs had similar structural information as compared to the CT DRRs. The spatial linearity of the CT and MR-images were then evaluated by measuring the percent distortion and spatial error; they also found out that there were no statistical differences in spatial linearity or accuracy in the two sets of images. Electron densities to the various volumes were assigned in the MR-image and a homogenous MR-based treatment planning of the head phantom was developed using the pinnacle treatment planning system. The dosimetric accuracy in the MR-based treatment planning was verified using lithium fluoride thermoluminescent dosimeter at various points in the phantom. It was concluded that for brain, MR-based homogenous treatment planning could be used with a dosimetric accuracy of ±2% (Ramsey and Oliver, 1998).

Chen et al (2007) also worked on MR-based treatment planning system using 20 prostate cancer patients. MR-images of the 20 patients were taken using 0.23 T MR-scanner and the corresponding CT images were also taken. In their work, Chen et al (2007) did a manual contouring of the bone and assigned a bulk density of 2.0 g/cm^3 and then generated a pseudo-CT. MR-based DRRs were generated and compared to the CT DRRs. The accuracies of the two DRRs were quantitatively evaluated for each patient using eight measuring points from which they concluded that the maximum difference in absolute positions was 3 mm and also a dosimetric accuracy of ±2% (Chen et al., 2007).

Eilertsen et al (2008) also investigated the dose calculation in an MRI-only workflow in RT dose planning using the bulk density override by fixed densities to different classes of tissues. The treatment planning was done with four sets of data namely: CT images 2, homogenous MR-images with no contouring of bone, homogenous MR-images with soft tissue of density 1.02 g/cm^3 and contoured bone with density 1.30 g/cm^3, homogenous MR-image with soft-tissue density set at 1.02 g/cm^3 and a contoured bone of 2.10 g/cm^3. The dosimetric accuracy was found to be ±1%, ±2.8%, ±1.6%, ±9.7% respectively. In this study, the images were classified into different tissue classes and the corresponding density values were assigned to them (Eilertsen et al., 2008).

Similar studies were done by Chin et al. (2014) and Johnstone et al. (2018). The only variation in the studies were that most of them assigned different electron density values to bone after contouring and that led to different dosimetric accuracies after treatment planning.

The major setbacks of this technique are that, since most of them were using T_2-imaging sequences, bone and air had the same signals and properties making it difficult to differentiate between them. Chin et al (2014) did bone contour on a CT image and transferred it onto the MR-images before assigning the bulk densities while others resorted to manual bone contouring which ended up to be time consuming and also unaccepted in the clinical field. Another setback was also the assumption that the body is homogenous, resulting in a lot of discrepancies in dose calculation of about 2% as compared to the heterogeneous CT planning (Chin et al., 2014).

2.8.2 Atlas-Based Technique

This is also another method of generating a pseudo-CT, in which an atlas is created by co-registering MR and CT images from a database of patients. For pseudo-CT generation, MRI data are co-registered to the atlas. Dowling et al (2012) worked on atlas-based electron density mapping method for MRI-only treatment planning system using 39 prostate cancer patients. An atlas was generated by co-registration the MRI and CT images and each patient image was registered to the atlas to generate a pseudo-CT image by the global and non-rigid registration method. A comparison in segmentation between the CT and pseudo-CT was made using the dice similarity coefficient and also dose calculations at each point for 26 patients were made. A dose difference of less than 2% was found, and a chi-squared test performed on the data indicated that the dose distribution in both pseudo-CT and CT planning were equivalent. (Dowling et al., 2012).

Dowling et al (2015) also worked on automatic substitute CT generation and contouring for MRI-only external beam radiation therapy from standard MRI sequence using a 3T MRI scanner on 39 patients with localized prostate cancer. Each patient's CT scan was co-registered to their whole pelvis T_2-weighted image using symmetric rigid registration and structure guided deformable registration. A new multi-atlas weighted voting method was used to generate automatic contour as pseudo-CT results. The mean error in HU between pseudo-CT and the corresponding patient CT was 0.6±14.7HU with an absolute error of 40.5±8.2HU (Dowling et al., 2015).

Other works by Siversson et al. (2015) generated similar results.

2.8.3 Voxel-Based Technique

Another option which could be explored to generate a pseudo-CT is the voxel-based technique. In this method, one or more specialized sequences such as the ultra-short echo time sequence (UTE) is used to create a pseudo-CT based on intensity variation. The technique does not require accurate image registration or segmentation if statistical methods are used (Johansson et al., 2012). In the work by Kapanen et al (2013), the authors evaluated the relationship between electron density and the intensity of the MR image using the voxel-based technique. In this study, Kapanen et al (2013) converted MRI intensity data to HU data for radiotherapy dose calculation. The experiment was conducted using 20 patients (10 patients for the experiment and another 10 to validate the process). Kapanen et al (2013) used 800 image voxels in the pelvis from the MR and CT images to generate a relationship between MRI intensity and the electron density from the calibrated HU-values. Out of the generated pseudo-CT images, it was concluded that the MRI intensity and the HU values had a direct relationship within a HU range of 0 to 1400 for pelvic bone and the dose calculation using the pseudo-CT was found to be accurate (Kapanen and Tenhunen, 2013).

CHAPTER THREE

METHODOLOGY

3.1 Patient Selection

The patient groups selected for this study were lung cancer patients and lymphoma patients from the St. Olavs Hospital in Trondheim, Norway. For the lung cancer patients, CT and MR images of the head were used and for the lymphoma patients, pelvis images were used. The study started with lung cancer patients and later extended to lymphoma patients because the MRI planer (the software that was used to generate the pseudo-CT) that was used to generate the pseudo-CT was made specifically for pelvic MR-images. The inclusion criteria for patients selected for the study were:

1. Patients with T_2-weighted images.
2. Patients with corresponding CT images.
3. Patient images included the abdominal part.
4. Patient images were fit in the field of view (FOV) for both MRI and CT images. For this reason, thin patients were considered.

Patients who did not satisfy the inclusion criteria were excluded from the study. Figure 4.19 in Chapter 4 shows an image of patient with parts of the body outside the FOV of the MRI system.

3.2 Image Acquisition

All the images used in this study were acquired from the St. Olavs Hospital. Two imaging modalities were used to acquire the images. The CT images were acquired with the biograph mCT PET/CT scanner whiles the PET and MR images were acquired using the biograph mMR PET/MR scanner. Both scanners were Siemens and were installed in 2013. The images comprised of CT and MRI. For the head MR images, ultrashort echo sequence (UTE) images were used to generate the μ-map since it came with bone. The patients used suffered from lung and lymphoma cancer and for diagnostic purposes, PET/CT and PET/MR were used for their examination. Before the examination, all the patients were injected with fluorodeoxyglucose (FDG) mostly an hour before examination. All patients were informed about the purpose of the study and therefore volunteered for their images to be used. All patients signed informed written consent prior to study entry.

3.2.1 Acquisition of Head Images

For the head images acquired from lung cancer patients, the ultrashort echo (UTE) and T_2-weighted sequences were used in imaging. The examination protocol included repetition time (*TR*) and echo time (*TE*) of 11.94 ms and 0.07 ms respectively, a field of view of 300 x 300 mm^2, a flip angle of 150°, slice thickness of 3.0 mm and 44 slices.

3.2.2 Acquisition of Pelvis Images

The pelvis or abdomen images were acquired on patients with lymphoma. For this, the DIXON and T_2-weighted sequence were used in the study. The examination protocol included repetition time (*TR*) and echo time (*TE*) of 3.60 ms and 1.23 ms respectively, a field of view of 3288 x 500 mm^2, a flip angle of 150° , slice thickness of 3.0 mm and 31 slices.

3.3 Image Processing

Image processing and modification were done on HP Pavilion g6 with 64-bit AMD A10-4600M CPU, clock speed of 2.30 GHz, 8 Gb installed RAM, and running on a Windows 10pro. The software used for viewing the images was Radiant DICOM Viewer and the software packages used for processing the images were MATLAB R2018b, statistical parametric mapping (SPM) and Elastix version 4.7.

Matlab was the scripting language used in this research for the image modification, image processing and graph plotting. The SPM and Elastix were toolboxes in Matlab for the image co-registration. Statistical parametric mapping (SPM) was also used to convert the digital imaging and communications in medicine (DICOM) to neuroimaging informatics technology initiative (NIFTI) files. To start processing and modification of the images, the first part of the image processing was to separate the head of the patient from the whole body CT. This was done by discarding the image slide from the shoulder downwards and this was done using the Radiant DICOM Viewer. The DICOM images were converted to NIFTI files to reduce the overall image processing time. DICOM images are stored as slices but the NIFTI format compresses all the slices into a single image unit, which is easier. This conversion was done with SPM. The next step for the image processing was to create region of interests (ROIs) around the head in each slide to mask away the surrounding noise or image seen around the head, and this was done in Matlab.

3.4 Conversion of Hounsfield Unit (HU) to PET Linear Attenuation Coefficients (LAC)

The major challenge encountered with using CT images for PET attenuation correction was limited to translating the HU values from the CT images to μ-values at 511 keV and also to μ-values for the photon spectrum of the linac. Theoretically, the performance of attenuation correction in PET is illustrated in Figure 6.

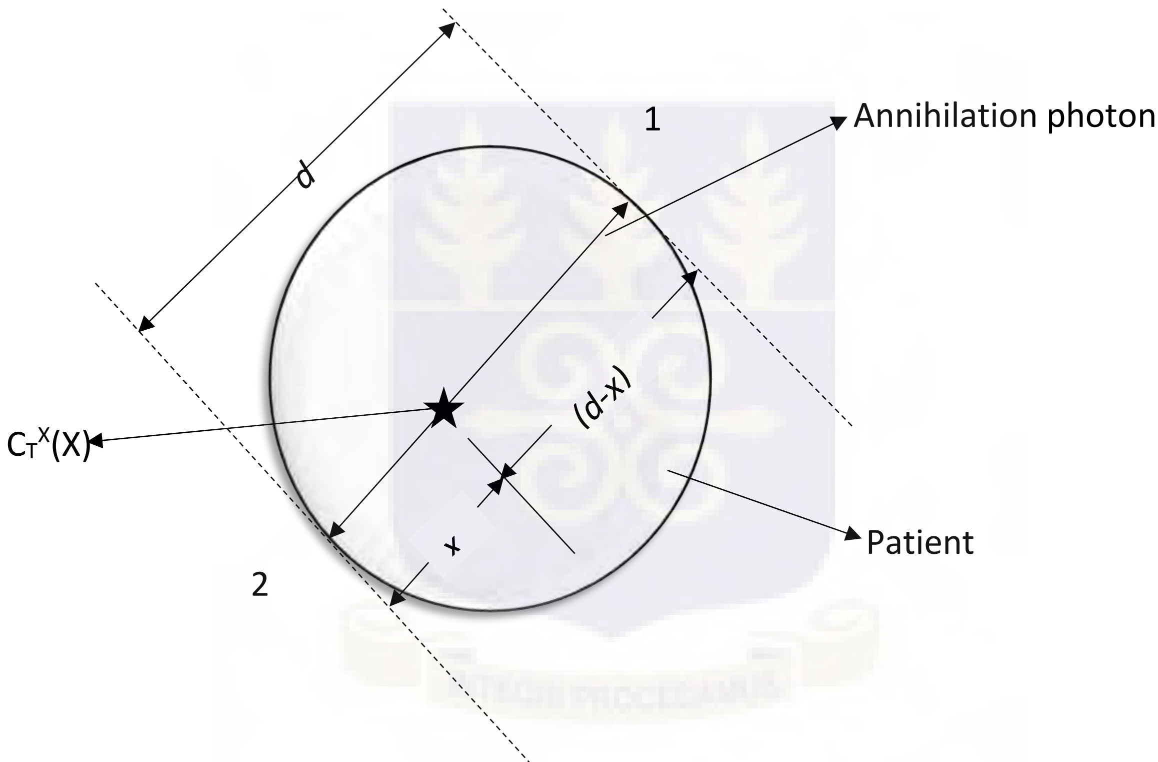

Figure 3.1: Annihilation process in the body of a patient.

with a positron to produce two photons at an angle 180° to each other. Assuming the radioactivity at the point of annihilation is C_T at the position *(x)*, the detector length at which the photon has to travel is *d*. so, one photon travels *x* and the other travel *(d-x)*.

For the probability of a photon reaching detector 1, P_1:

Signal in detector 1 is given by $s_1 = C_T(x)\, e^{-\mu(d-x)}$ (Eqn 3.1)

Assuming the body is homogenous, therefore linear attenuation is constant.

Therefore probability of a signal arriving at detector 1 is given by $P_1 = \frac{s_1}{C_T(x)^x}$ (Eqn 3.2)

For the probability of a photon reaching detector 2, P_2:

Signal in detector 2 is given by $s_2 = C_T(x)\, e^{-\mu(x)}$ (Eqn 3.3)

Therefore probability of a signal arriving in detector 2 is given by $P_2 = \frac{s_2}{C_T(x)^x}$ (Eqn 3.4)

So probability of a signal reaching a detector is given by equation 3.4 which is the number of photons detected divided by the activity in the tissue.

From chapter 2, attenuation was defined as the probability of detecting the photon pair, which means we have to multiply P_1 andP_2 as defined in equation 3.5.

$$P_1 P_2 = e^{-\mu x} e^{-\mu(d-x)} \quad \text{(Eqn 3.5)}$$

Therefore the total signal detected is $S=P_1.P_2.C_T$

$$S = e^{-\mu x} e^{-\mu(d-x)} C_T \Longrightarrow S = C_T(x) e^{-\mu d} \quad \text{(Eqn 3.6)}$$

The equation 3.6 is valid for only a homogenous body and for the total signal to be calculated, we need: we need to know how thick the body is along the line of coincidence, and the amount of signal that has been attenuated.

But for a heterogeneous body, since attenuation varies along the line of incidence then we have to integrate to get equation 3.7 which is a continuous distribution of attenuation.

$$S = C_T(x) e^{-\int \mu d} \quad \text{(Eqn 3.7)}$$

Theoretically, the above method is the method that can be used for attenuation. Meanwhile in this research, the conversion method used by (Carney et al., 2006) was adopted as described in the figure 3.2, he used two slopes on each side of the breakpoint, the technique involved the use of two slopes on each side of the breakpoint; the conversion function was bilinear with slopes coefficients listed in table 3.1, peak voltage used for the images was 120 keV.

Table 3.1: Coefficients a and b for various slopes described in the Figure 3.2, the break points, and their corresponding peak voltages for the conversion of HU to PET LAC as described by Carney et al. (2006)

Peak Voltage (kV)	**a ($\times 10^{-5}cm^{-1}$)**	**b ($\times 10^{-2}cm^{-1}$)**	**BREAK POINT(BP) (HU+1000)**
80	3.64	6.26	1050
100	4.43	5.44	1052
110	4.92	4.88	1043
120	5.10	4.71	1047
130	5.51	4.24	1037
140	5.64	4.08	1030

.

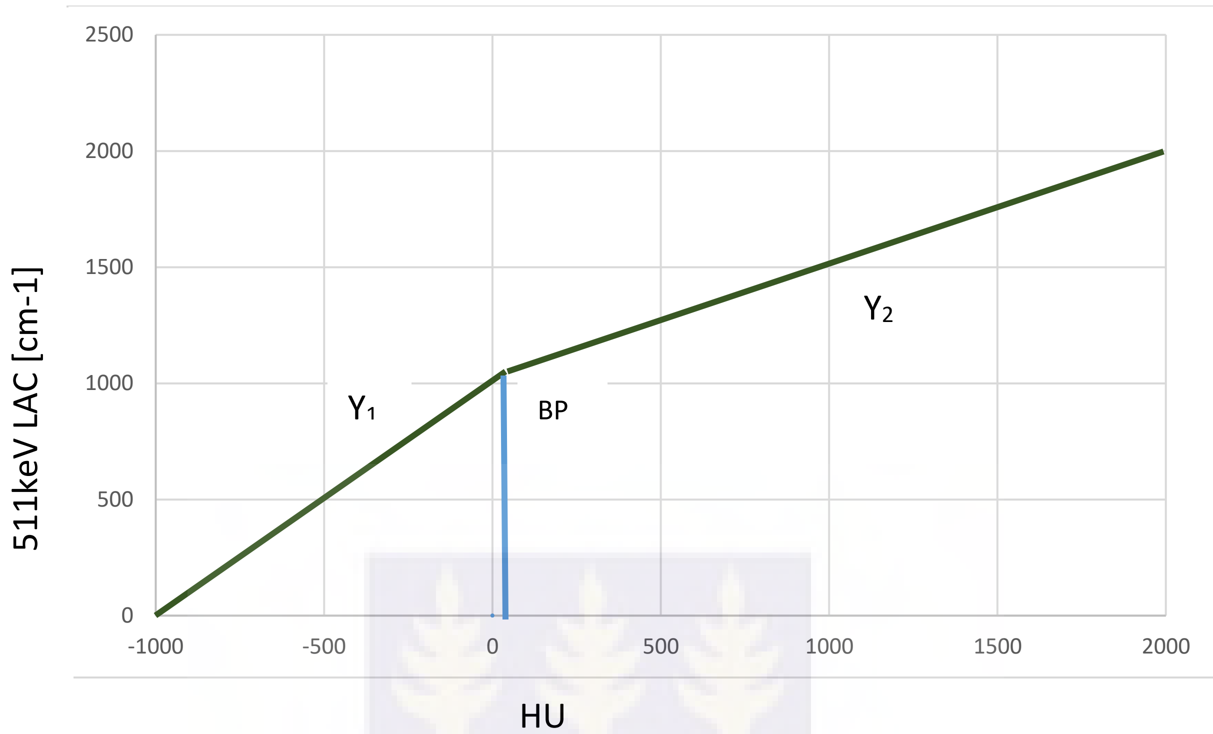

Figure 3.2: A bilinear conversion function between HU and 511 keV LAC as described by Carney et al. (2006).

For the images in this study, the peak voltage used was 120 kV with a breakpoint at 47 HU and the various a and b coefficients as indicated in the Table 3.1. Therefore according to Carney et al. (2006), the slopes were estimated using equation 3,8 and 3.9:

$$y_1 = [9.6 \times 10^{-5}(HU + 1000) \quad \text{(Eqn 3.8)}$$

$$y_2 = [a(HU + 1000)+b]cm^{-1} \quad \text{(Eqn 3.9)}$$

3.5 µ-Map Creation

As described earlier in chapter 1, the main objective of this research was created different mu-maps from MR-based and pseudo-CT techniques and compared them at varying thresholds or parameters for radiotherapy and PET/MR, different μ-maps were created depending on the images (patients) and later compared using various parameters.

3.5.1 Pseudo CT Creation

The MRI-planner (software used to generate the pseudo-CT) was created by a team in Sweden whose main aim was to facilitate the use MRI only in radiotherapy for successful tumor treatment and minimal side effect (Siversson et al., 2015). The system used to generate the pseudo-CT is still a work-in-progress and therefore can only be used for research and not for clinical purposes. The MRI planner is a special tool that is used to create synthetic CT images from standard MR images using statistical decomposition algorithm. This software is an advanced machine learning technology which was built on the foundation of atlas-based method of attenuation correction as described in Chapter two section 2.6.2. The process involved is to upload the T2 weighted images into the online server and wait for a couple of hours for the pseudo-CT to be generated. The result of the pseudo-CT is discussed in chapter 4.

3.5.2 MR μ-Map Generation

The MR μ-map generation was done using the Siemens software at the PET center of St Olav hospital Trondheim. The software came with the PET/MR machine and is developed by the developers from Siemens. The software is a machine learning technology that uses MR-images produced by the PET/MR to generate a μ-map that is used for attenuation correction in PET. In most cases, the software gives options where bone is added to the μ-map. This software has been in use since 2013 and is very efficient for μ-map generation.

3.5.3 CT at 511 keV μ-Map Generation

For the head μ-map creation, three set of images were used, the whole body CT image, MR T_2 weighted images and MR- μ-map. The whole-body CT image was cropped to discard images from the neck downward, regions of interest (ROIs) were created on each slide and then masked on the CT-HEAD to do away with the noise surrounding the image, result was save as masked CT-HEAD, and were then registered to the MR T_2 weighted images using both SPM and Elastix, resulting image was saved as "registered CTMR". The registered CT-HEAD and MR T_2 weighted were then converted using a bilinear conversion function from HU to 511keV PET LAC as described by Carney et al. (2006)., the resulting image was saved as 130_511 and 124_511.

CHAPTER 4

RESULTS AND DISCUSSION

4.1 Results from Head Studies

4.1.1 Image Processing

The figure 4.1 shows two images before and after image processing. From figure 4.1 (A), it is observed that the arm of the patient on each side of the head, due to the positioning of the patient, and also the presence of other artifacts make the image registration difficult to be done.

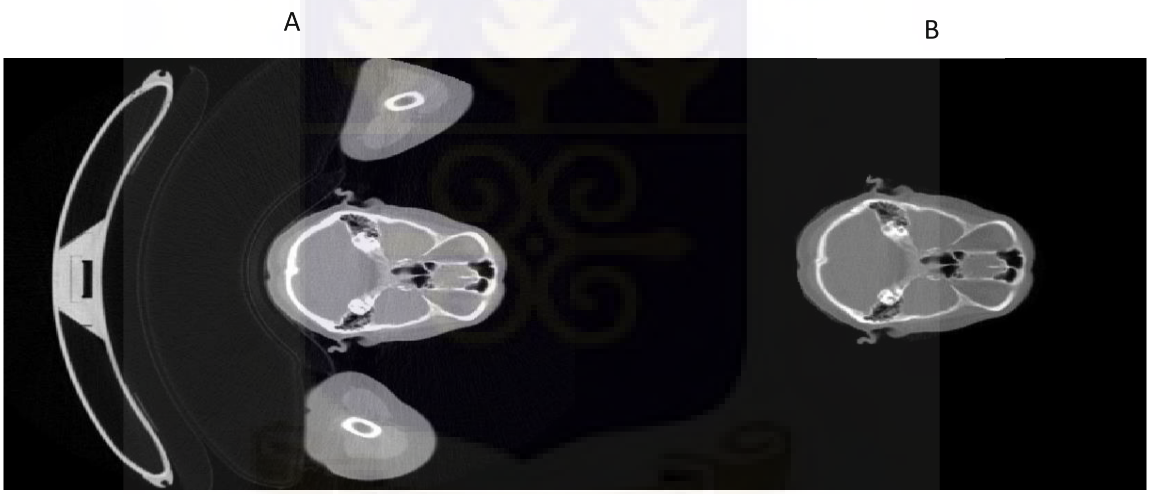

Figure 4.1: A CT image before (A) and after (B) processing.

4.1.2 Image Registration

For the SPM, there was an interface where the reference image and the source image were uploaded and then co-registered. Results obtained from the SPM were not satisfying enough. The SPM provided the option to check the result of the registration but all the time it was far from good. Below are images showing results obtained from some of the co-registration done with SPM.

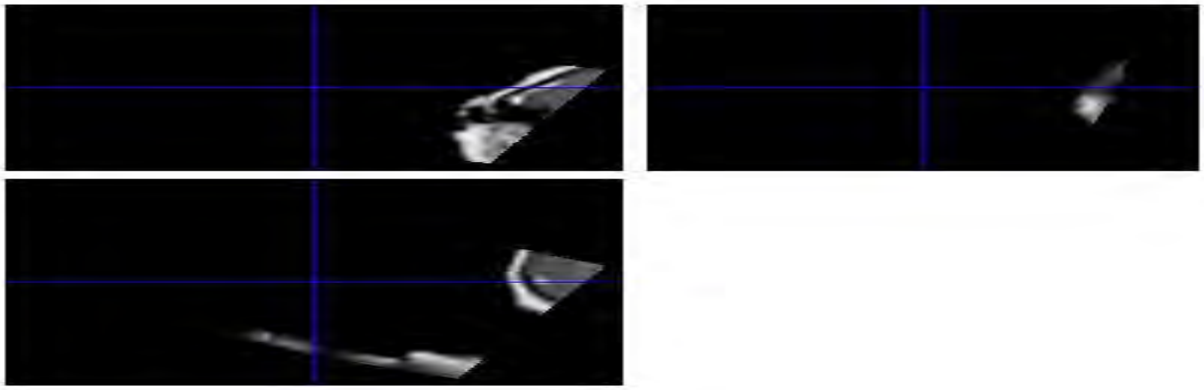

Figure 4.2: Failed co-registration between CT and MRI using SPM.

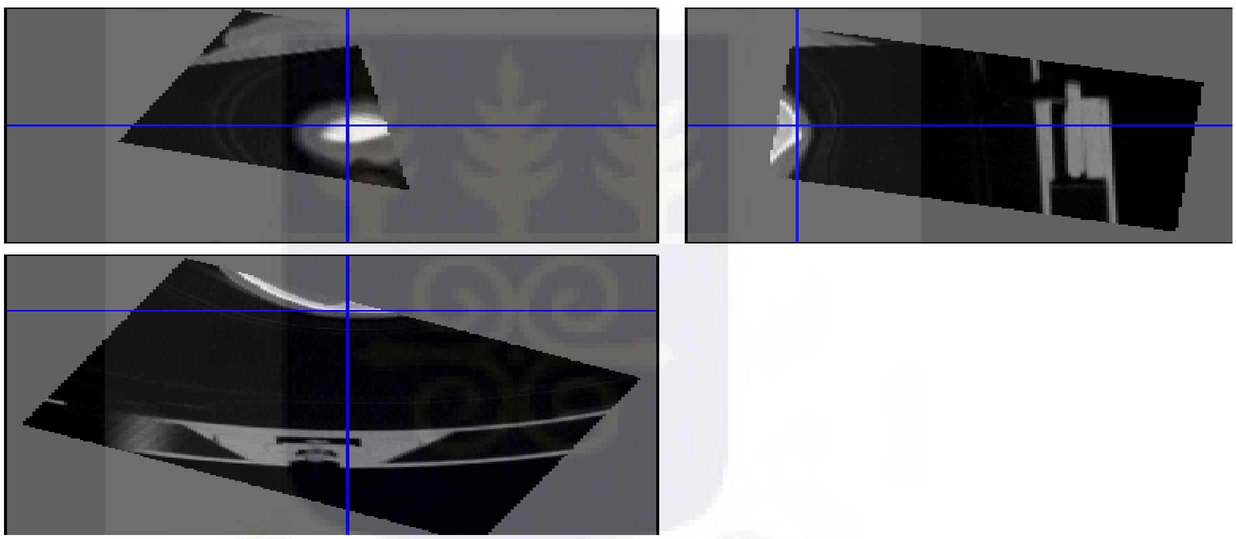

Figure 4.3: Failed co-registration between CT and MRI using SPM

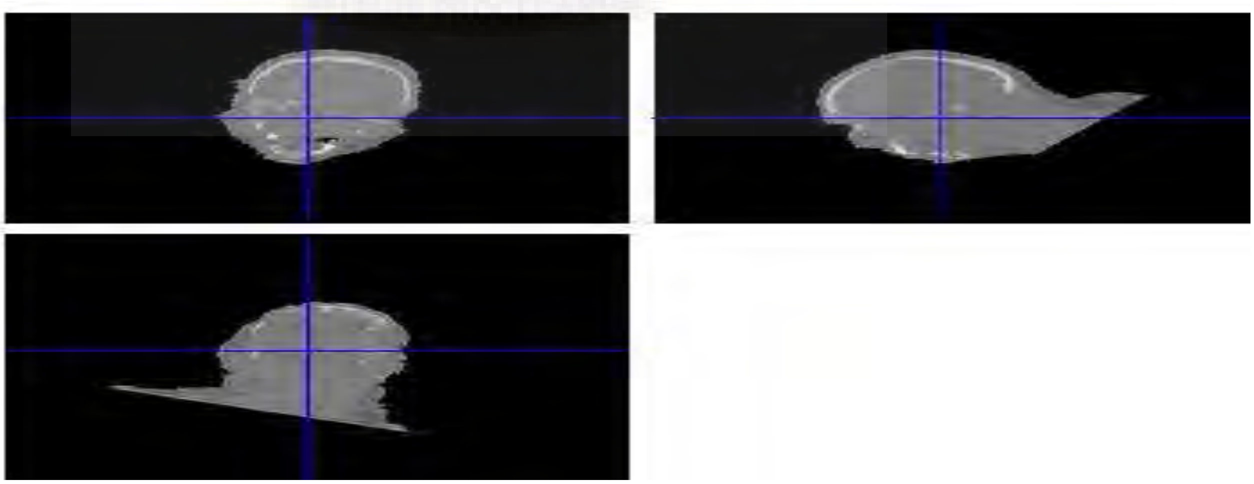

Figure 4.4: Failed co-registration image between CT and MRI using SPM.

From the above images (Figure 4.2-4.4) it was clearly shown that the coregistration in Figure 4.2 and 4.3 failed completely, Although Figure 4.4 looked a little good, it also failed the justification process where the registration is checked by comparing the CT and MRI images as shown in Figure 4.5. It was observed that a point in the brain of the MRI could be seen in the image corresponding to a different point in the CT image. This is why such registration was discarded.

Figure 4.5: Images showing the CT and MRI and how they did not have any corresponding points during the co-registration

Elastix image co-registration tool was chosen for the study. Elastix is a Matlab incorporated image co-registration tool that was used for the image registration. What makes the tool stand out is that it gives a lot of options to change most of the parameters until a good registration is done. For Elastix, the fixed image, moving image and the output directory were set and necessary changes made in the registration parameter file which was saved in plain text file (.txt) in Matlab. Some of the parameters that could be changed were the metric, transform method, resolution, number of interpolations, and number of samples to draw. After the registration was justified using SPM and also the image viewer in Matlab, as shown in Figure 4.6, it was clearly shown that a point chosen in the CT image corresponded to the same point in the MRI.

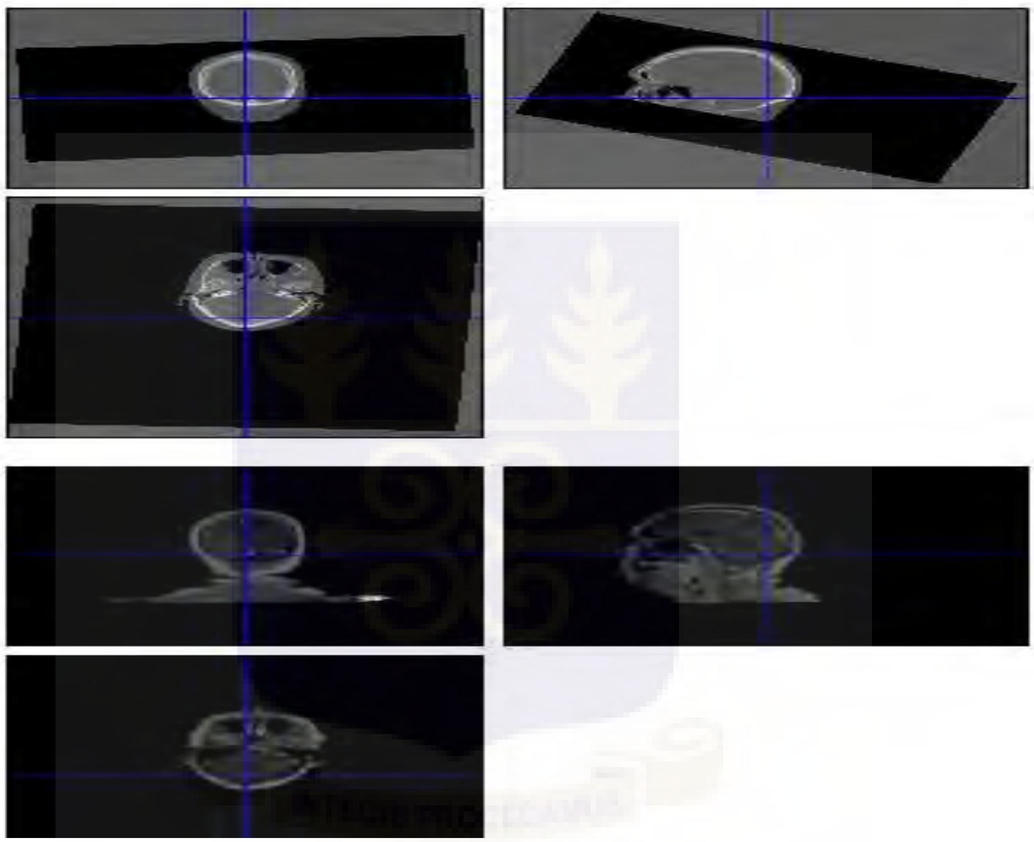

Figure 4.6: Registration in Elastix was justified by picking a point in CT image and seeing if it corresponded with the same point in the MR image

4.1.3 Conversion of Hounsfield Unit (HU) to PET Linear Attenuation Coefficient (LAC)

The conversion of HU to PET LAC was done using a bilinear conversion as shown by Carney et al (2006). A function was created in Matlab named HU2PETLAC.m using the relationship shown by Carney et al (2006) to convert CT image volume with voxel values in HU to 511 keV LAC μ-maps. The Figure 4.7 and 4.8 show CT images with voxel values in Hounsfield units and the same image which was converted to 511 keV PET LAC. After the conversion, a sharp brightness in the image was observed in the 511 keV PET LAC image as compared to the image before.

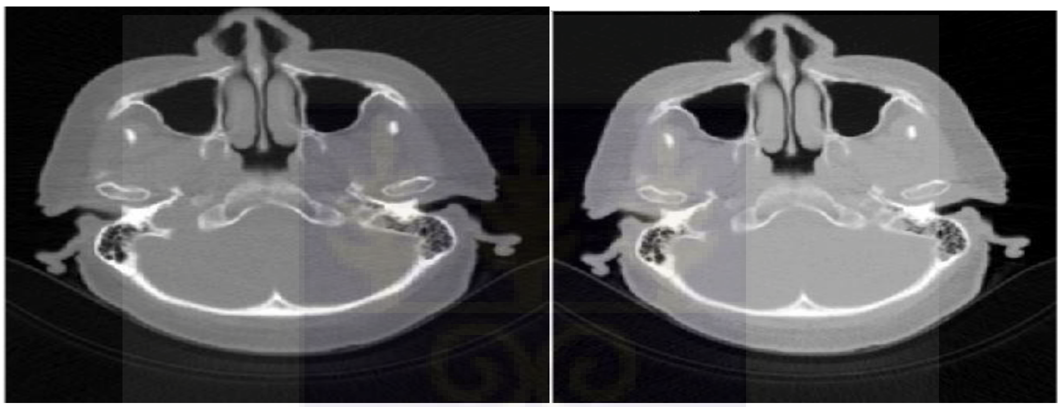

Figure 4.7: CT images with voxel values in Hounsfield units (left) and the same image which was converted to 511 keV PET LAC (right)

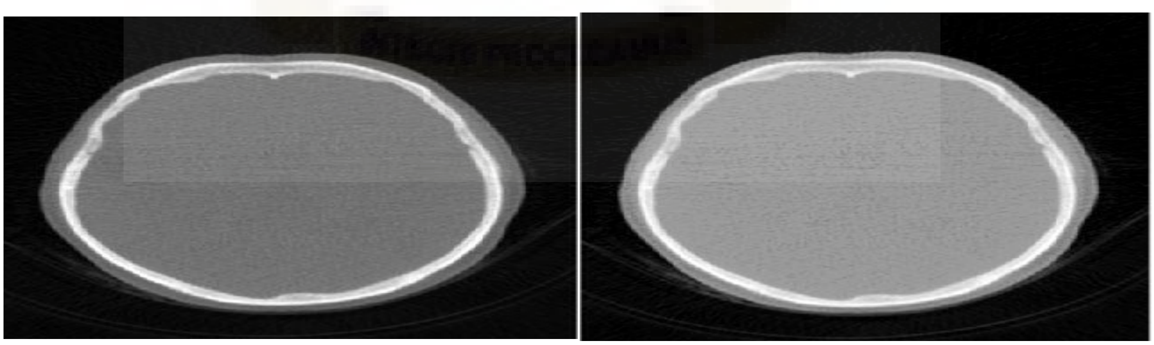

Figure 4.8: CT images with voxel values in Hounsfield units (left) and the same image which was converted to 511 keV PET LAC (right)

4.2.4 CT at 511 keV μ-Map Vs MR-Based μ-Map

To analyse the μ-map very well, various comparisons were made. The image analysis was initially done qualitatively by comparing each slide of the CT at 511 keV μ-map with its corresponding slide in the MR-based μ-map. From the visual observation, it was found that there were overestimation of bone in most parts of the images in the MR-based μ-map as compared to the CT at 511 keV μ-map as shown in Figure 4.9 and 4.10. Also, for some parts, there were underestimation of bone as shown in Figure 4.11 and 4.12. In general, it was observed that there was more bone overestimation in the MR-based μ-map than it being under-estimated. The overestimation and underestimation of bone in the images are made visible with the red circles in some selected slides from patients 130 and 124 in the Figures 4.9, 4.10, 4.11, and 4.12.

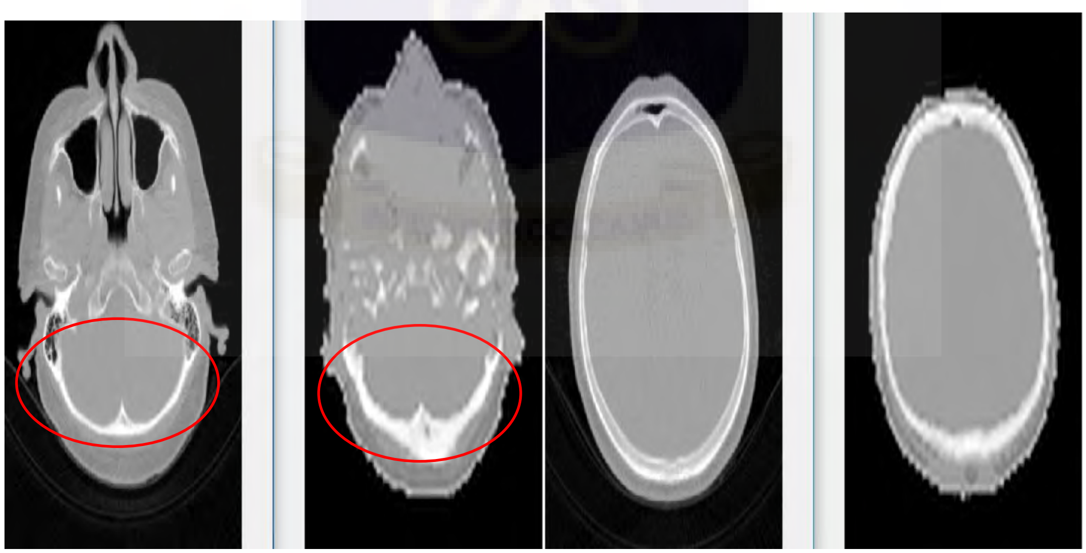

Figure 4.9: Images illustrating overestimation of bone in patient 130

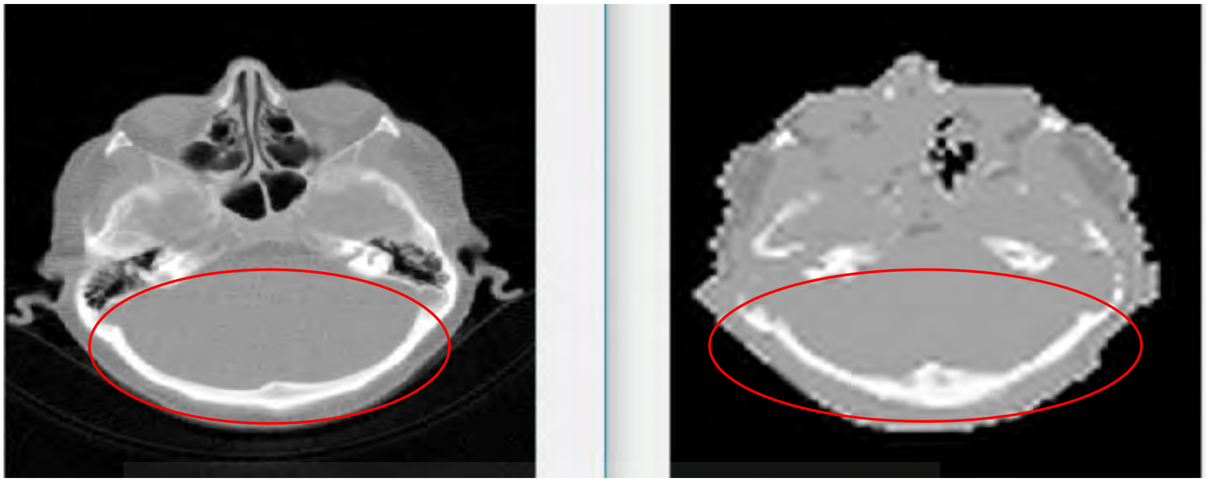

Figure 4.10: Images illustrating overestimation of bone in patient 124

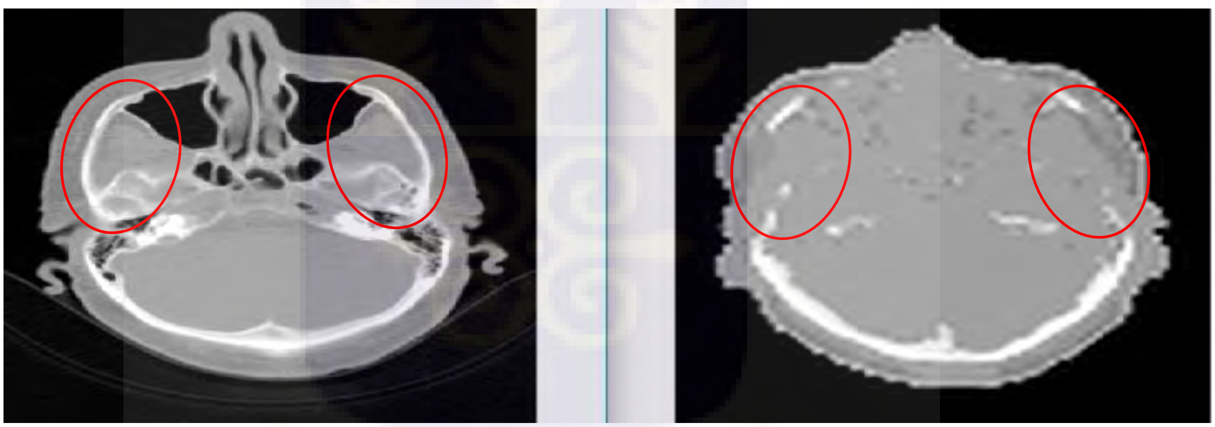

Figure 4.11: Images illustrating underestimation of bone in patient 130.

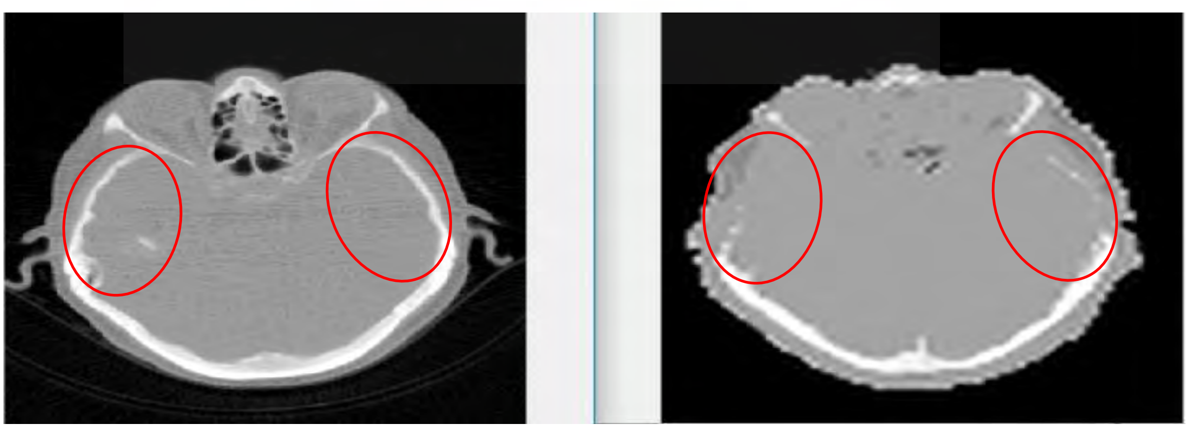

Figure 4.12: Images illustrating underestimation of bone in patient 124.

4.1.5 New Scatter Plots of CT at 511 keV μ-Values Vs MR-Based μ-Values

To analyse the CT at 511 keV μ-map and the MR-based μ-map, their μ-maps was plotted against each other; over 10,000 μ-values in the μ-maps were plotted and it was observed that an approximate linear relationship existed between them as shown in Figure 4.13 and 4.14. This shows that most points that were picked in the CT at 511 keV μ-map had a similar value in the MR-based μ-map. This means that the MR-based μ-map could be used to correct for attenuation in the absence of the CT at 511 keV μ-map.

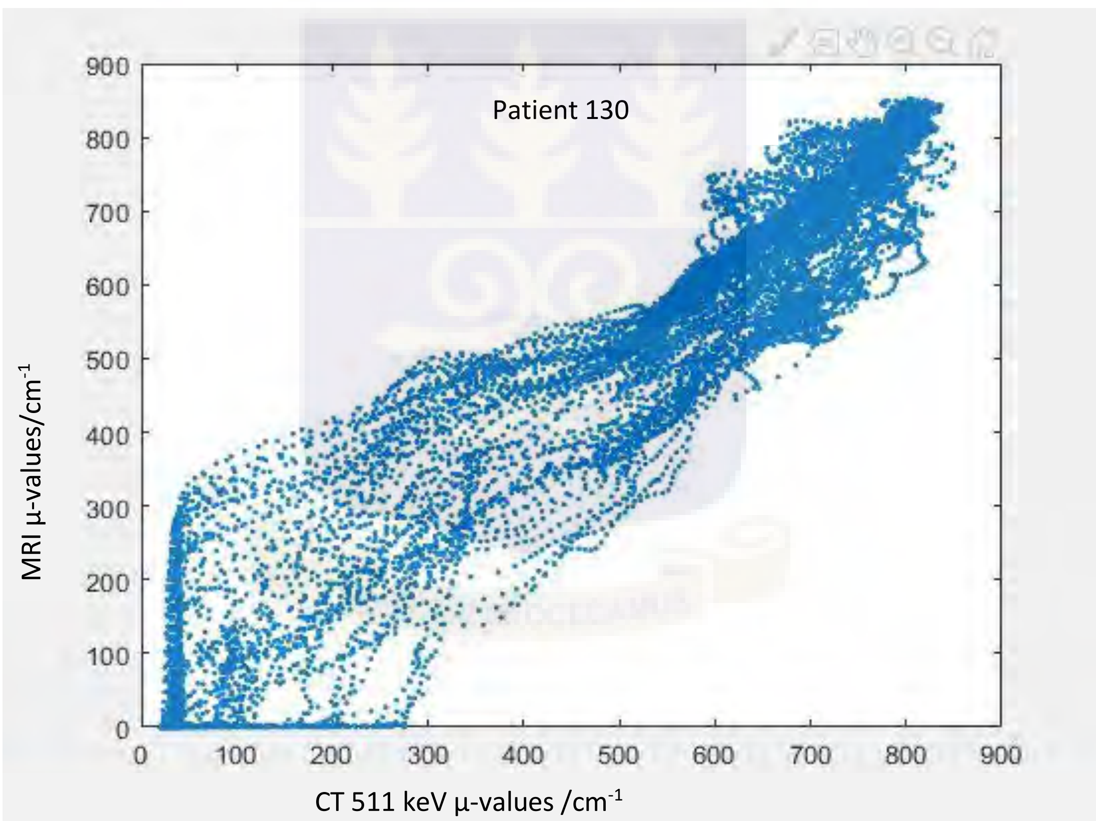

Figure 4.13: Scatter plots of CT at 511 keV μ-values against MR-based μ-values for patient 130.

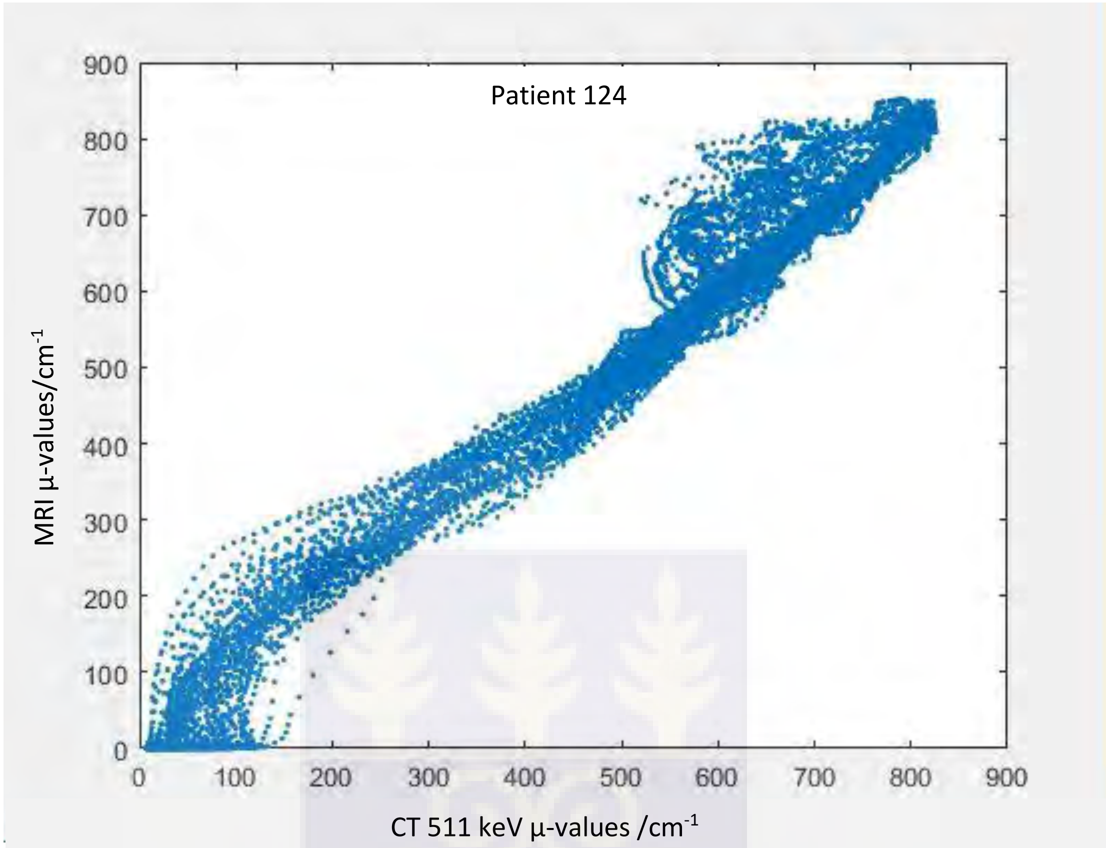

Figure 4.14: Scatter plots of CT at 511 keV µ-values against MR-based µ-values for patient 130.

4.1.6 BONE VOLUME PLOTS

It was found that for both patients (patients 130 and 124), the volume occupied in the MR-based µ-map was greater than the one in the CT µ-map. For patient 130, bone volumes of 2357 cm^3 and 2456 cm^3 for CT µ-map and MR-based µ-map respectively were observed. The difference was found to be 99 cm^3 as shown in Figure 4.15 representing 4.04% increase in bone volume. For patient 124, bone volumes of 2254 cm^3 and 2345 cm^3 for CT µ-map and MR-based µ-map respectively were observed. The difference was found to be 91 cm^3 as shown in Figure 4.16 representing 4.04% increase in bone volume.

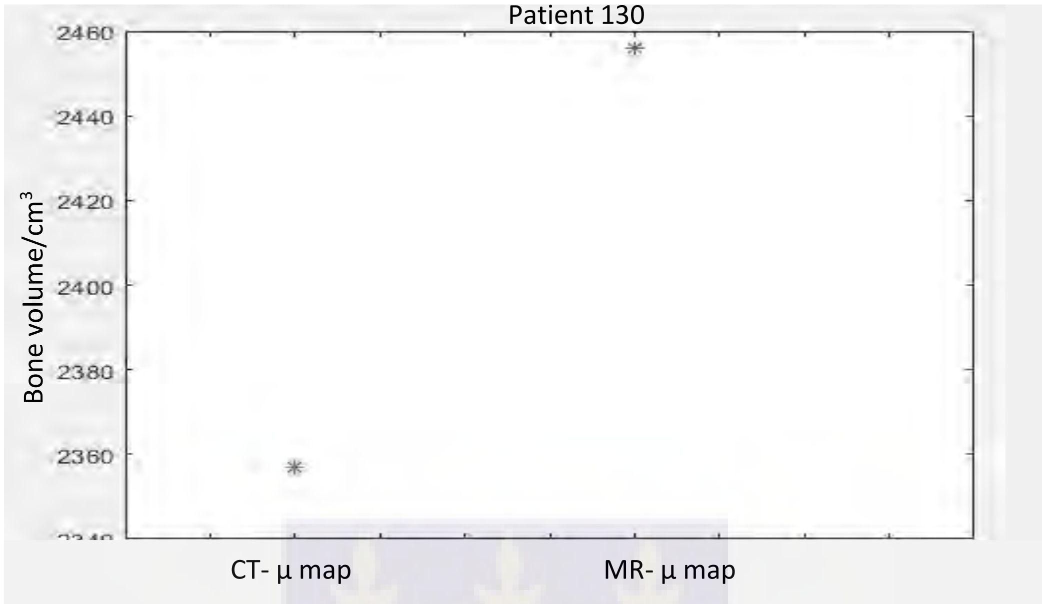

Figure 4.15: Comparison of the bone volume of CT µ map and MR-based µ map for patient 130.

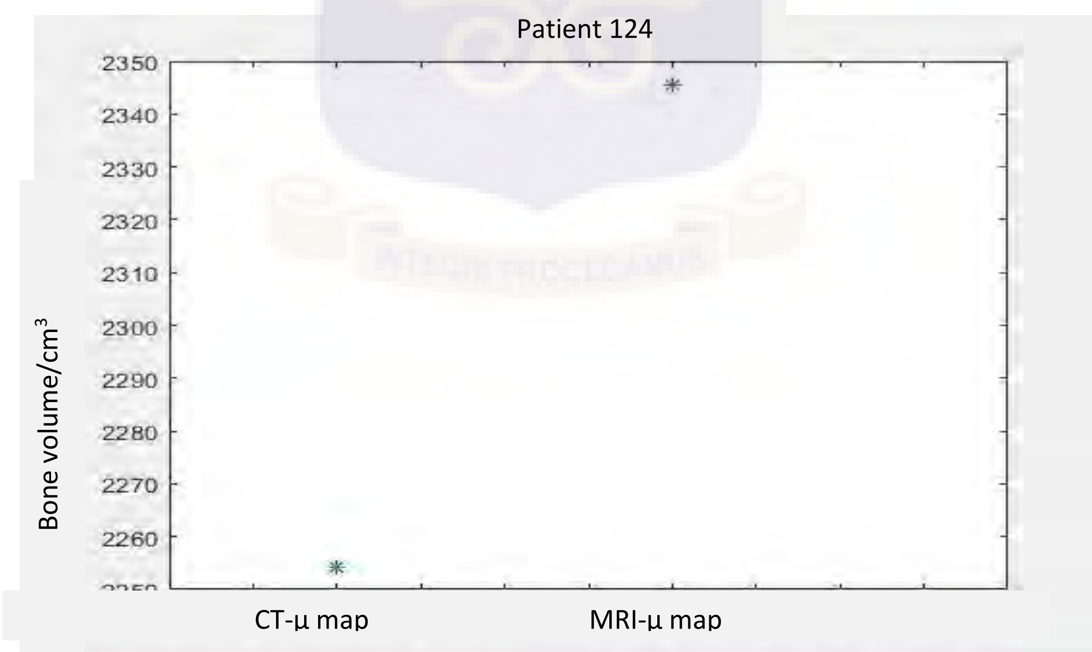

Figure 4.16: Comparison of the bone volume of CT µ map and MR-based µ map for patient 130.

4.1.7 Box Plot of μ-Values in the Bone Volume

The other comparison that was made in this study was to evaluate the variation in the μ-values of bone in the bone volume. This was done using Matlab by writing a script to generate a box plot. For patient 130, 271911 μ-values in bone were ploted and the median μ-values were 0.1396 cm^{-1} and 0.1468 cm^{-1} for CT μ-map and MR based μ-map respectively. From figure 4.17, it was observed that there was not much variation in the μ-values for both CT μ-map and MR-based μ-map. it was observed that a finite number of outliers were estimated at 410 and 135 for CT μ-map and MR-based μ-map respectively. For patient 124, 300000 μ-values in bone were plotted and the median μ-values were 0.1460 cm^{-1} and 0.1461 cm^{-1} for CT μ-map and MR-based μ-map respectively. From Figure 4.18, it was observed that there is not much variation in the μ-values for both CT μ-map and MR-based μ-map. It was observed that a finite number of outliers were estimated at 104 and 264 for CT μ-map and MR based μ-map respectively.

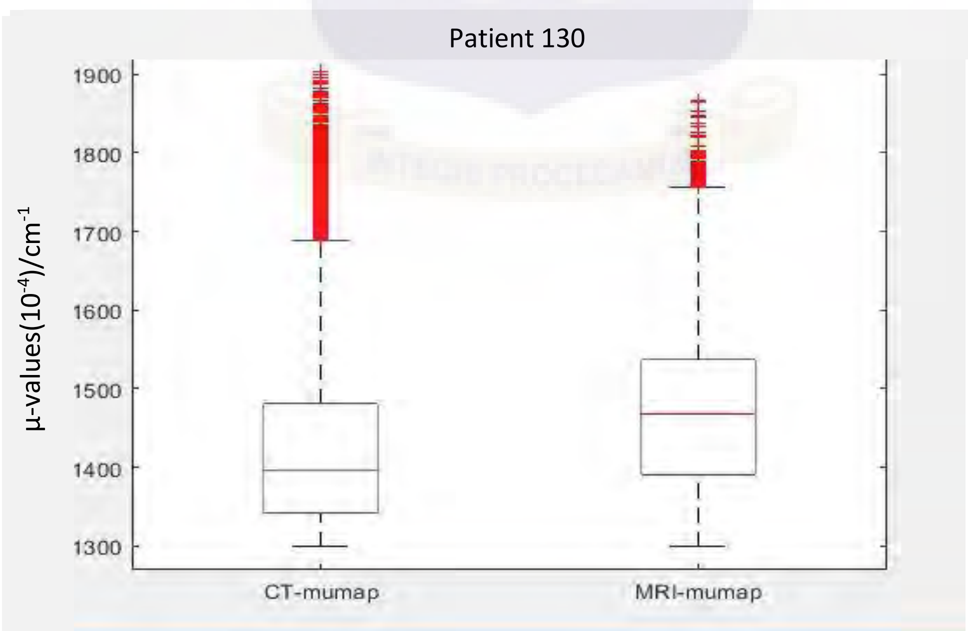

Figure 4.17: Box plot showing the variation of μ-values in the bone volume for patient 130

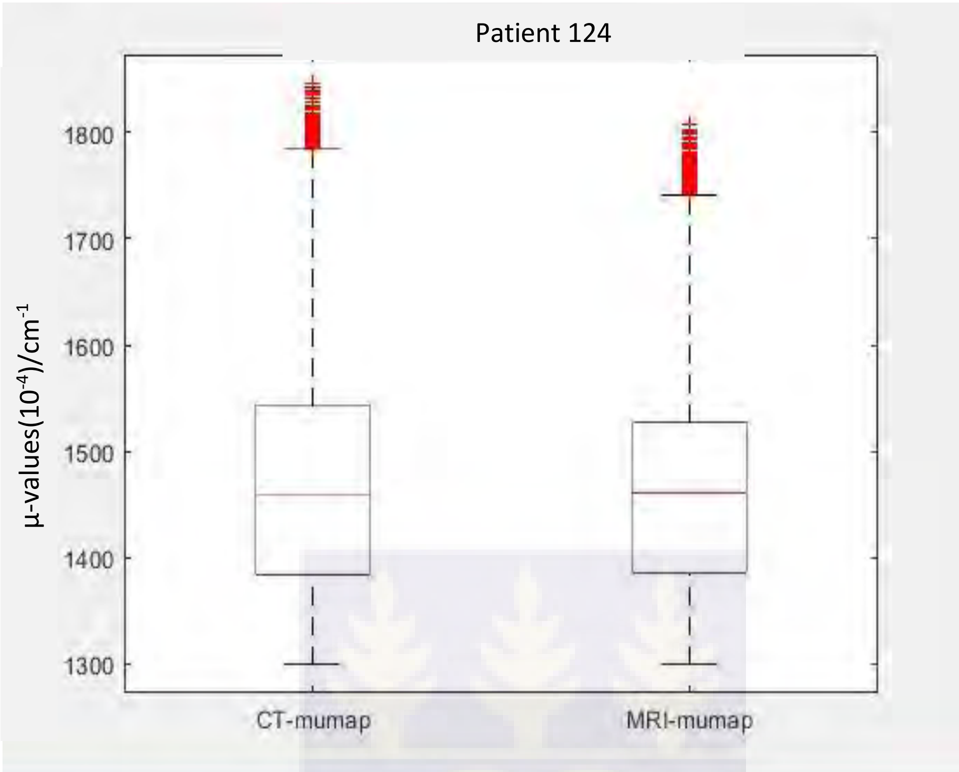

Figure 4.18: Box plot showing the variation of μ-values in the bone volume for patient 130

4.2 Results from Pelvis Studies

4.2.1 Patient Selection

The patient whose field of view fell outside that of the MRI were not considered for this study because the MRI planner is a machine learning tool and needed the outer part of the patient to model, correct and generate the pseudo CT. Figure 4.19 shows two patients (A and B), images of patients A was rejected because the outer part of the patient did not appear in the image, unlike the image of patient B, which has the outer part captured thus the MRI planner was able to generate the pseudo CT. This was a major selection criteria used in the selection of patients for this research work.

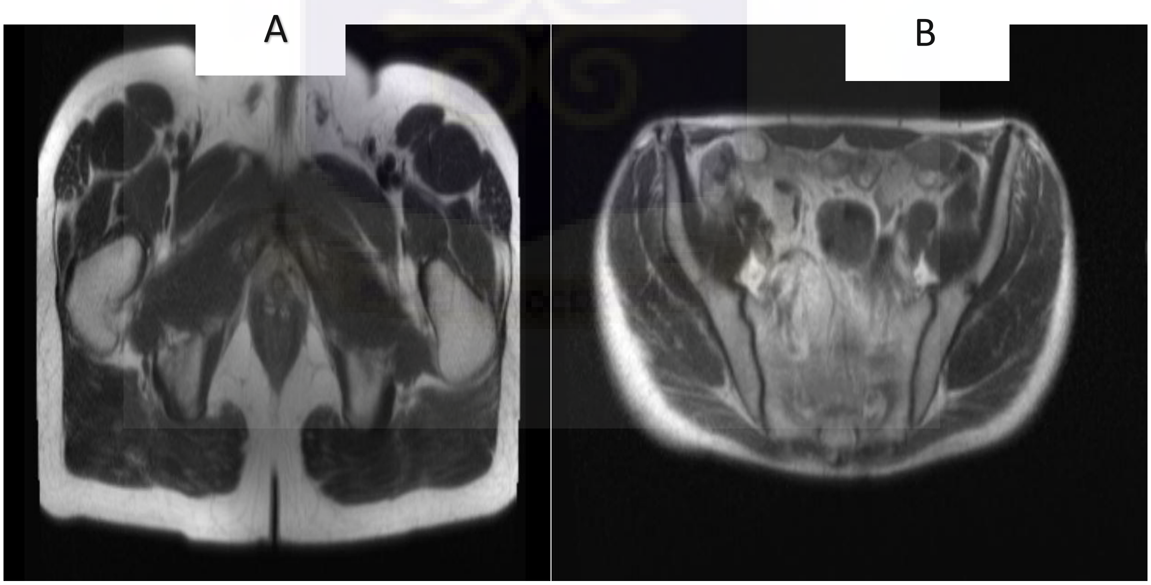

Figure 4.19: Images of two patients: one that didn't meet selection criterion (A) and one that met selection criterion (A)

4.2.2 Image Processing

The abdominal images were also processed to make them ready for this study. First with the help of Radiant DICOM Reader the body above the pelvis was discarded to help focus the study on only the abdominal part and also enhance the image co-registration. Also, to make the work easier, all DICOM files were converted to NIFTI files. This process was done so that the images could be accessed as one file and not a set of slides as presented by DICOM. The surrounding images which constitute noise were also removed by creating ROIs around the pelvis and later masking it on the pelvis images. This process was done in Matlab. Figure 4.20 shows before and after the image process was done.

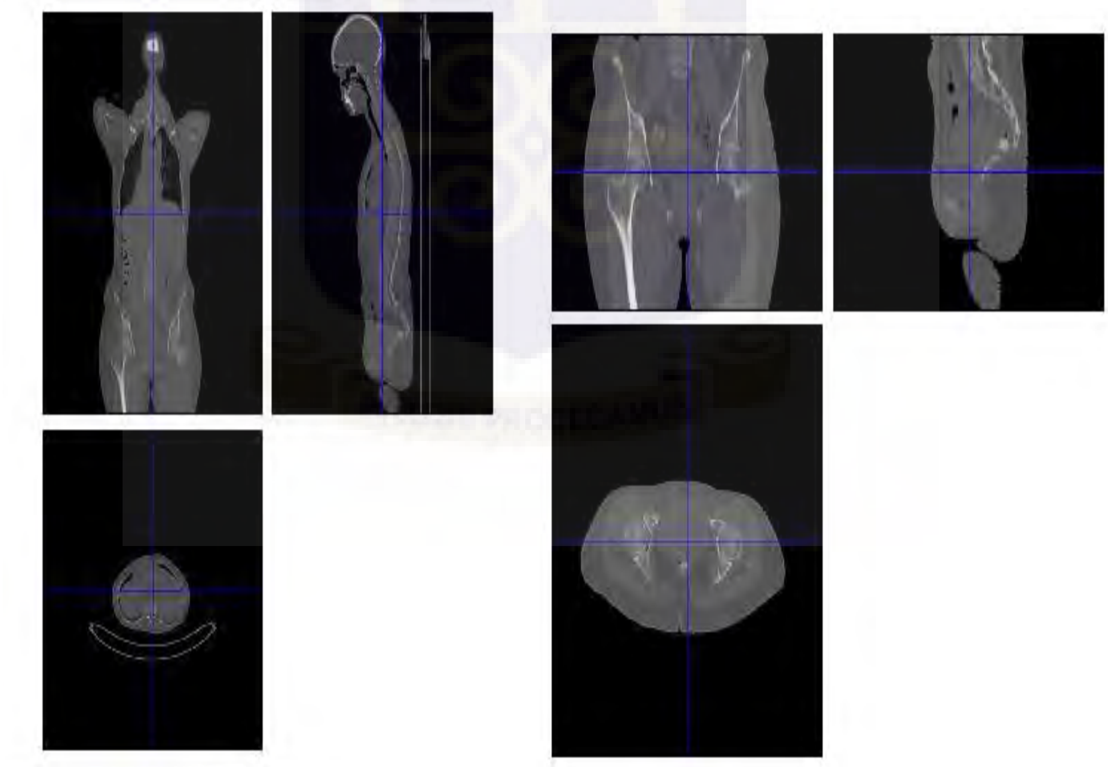

Figure 4.20: The pelvis before image processing (left) and after image processing (right).

4.2.4 Conversion of HU to PET LAC

A scale factor of 10^4 was used to multiply the LAC to increase the linear attenuation values for easy comparison. Figure 4.21 indicates before and after the conversion was made. A sharp brightness in the image was observed.

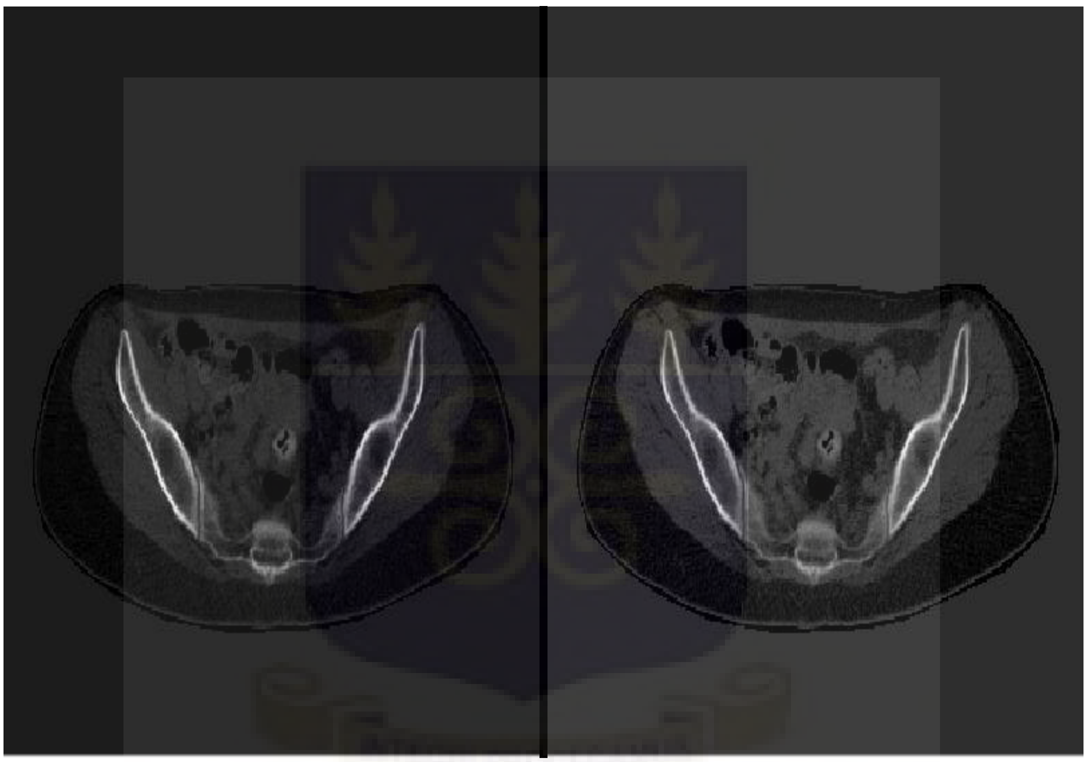

Figure 4.21: Before and after conversion of HU to PET LAC.

4.2.5 Comparison between CT- μ-Map, MRI- μ-Map and Pseudo-CT for Bone

The first part of the comparison was to evaluate the bone volume in all the three μ-maps. For this to be done, a script was written in Matlab to extract the bone from the whole abdominal part in the image, after this, the volume ocupied by the bone was calculated using DICOM information of the varrious images. Since a DIXON sequence was used for the imaging of the MR-images, bone was not part of the images so the comparison for bone was done between the CT- μ-map and the psuedo-CT all at a peak voltage of 511 keV. For patient 1, bone volumes of 850 cm^3 and 691 cm^3 were estimated for CT μ-map and the psuedo-CT respectively at 511 keV with a difference of 159 cm^3 as shown in Figure 4.22 representing 18.7% decrease in bone volume. For patient 2, bone volumes of 1200cm^3 and 945cm^3 were estimated for CT- μ-map and the psuedo-CT respectively at 511keV with a difference of 255cm^3 as shown in Figure 4.23, representing 21.3% decrease in bone volume. For patient 3, bone volumes of 721cm^3 and 652cm^3 were estimated for CT- μ-map and the psuedo-CT respectively at 511 keV with a difference of 70 cm^3 as shown in the figure 4.24, representing 9.6% decrease in bone volume, For patient 4, bone volume of 945 cm^3 and 812 cm^3 were estimated for CT- μ-map and the psuedo-CT respectively at 511 keV with difference of 133 cm^3 as shown in figure 4.25, representing 14% decrease in bone volume. For patient 5, bone volume of 1023 cm^3 and 921 cm^3 for CT- μ-map and the psuedo-CT respectively at 511 keV with difference of 102 cm^3 as shown in the figure 4.26, representing 10% decrease in bone volume. With the CT- μ-map being the gold standard, it was observed that the pseudo-CT underestimated the bone in the image, therefore leading to lower bone volume in all the images.

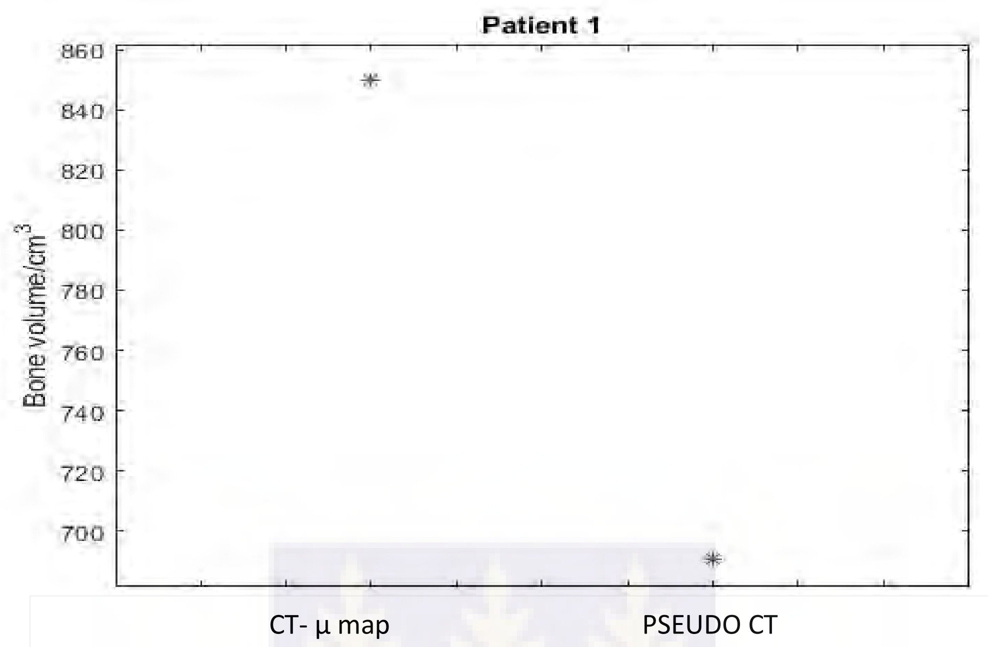

Figure 4.22: Comparison of the bone volume of CT µ-map and pseudo-CT for patient 1.

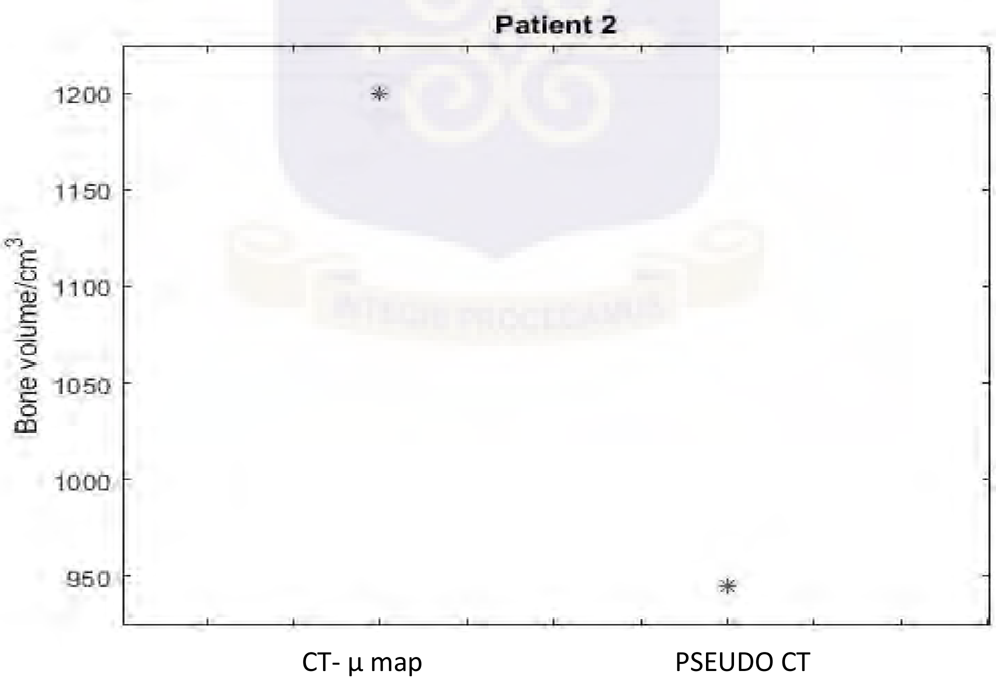

Figure 4.23: Comparison of the bone volume of CT µ-map and pseudo-CT for patient 2.

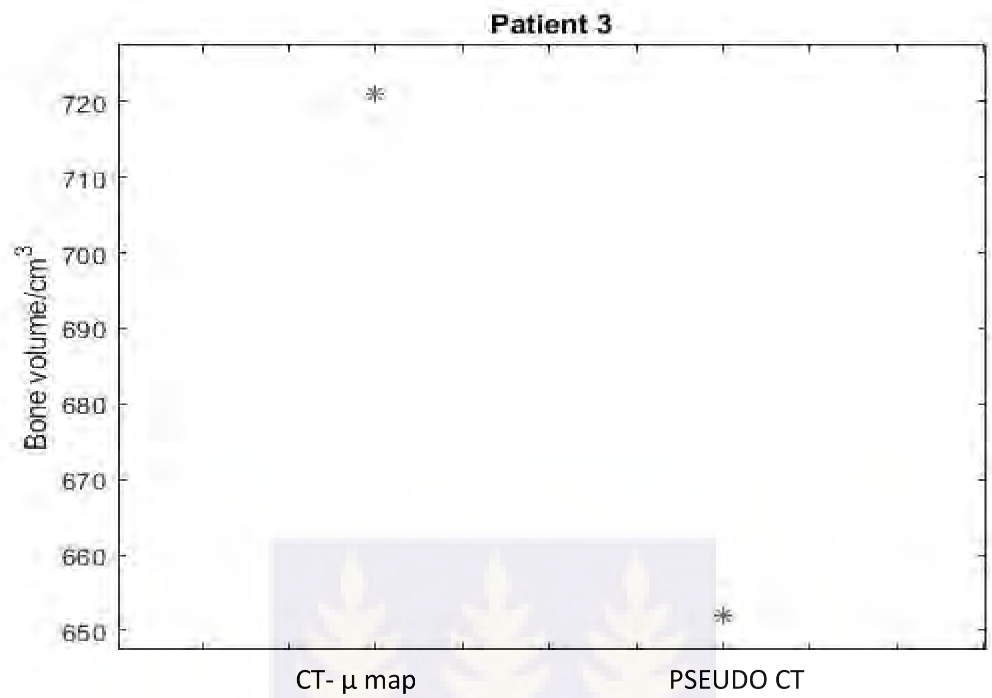

Figure 4.24: Comparison of the bone volume of CT µ-map and pseudo-CT for patient 3.

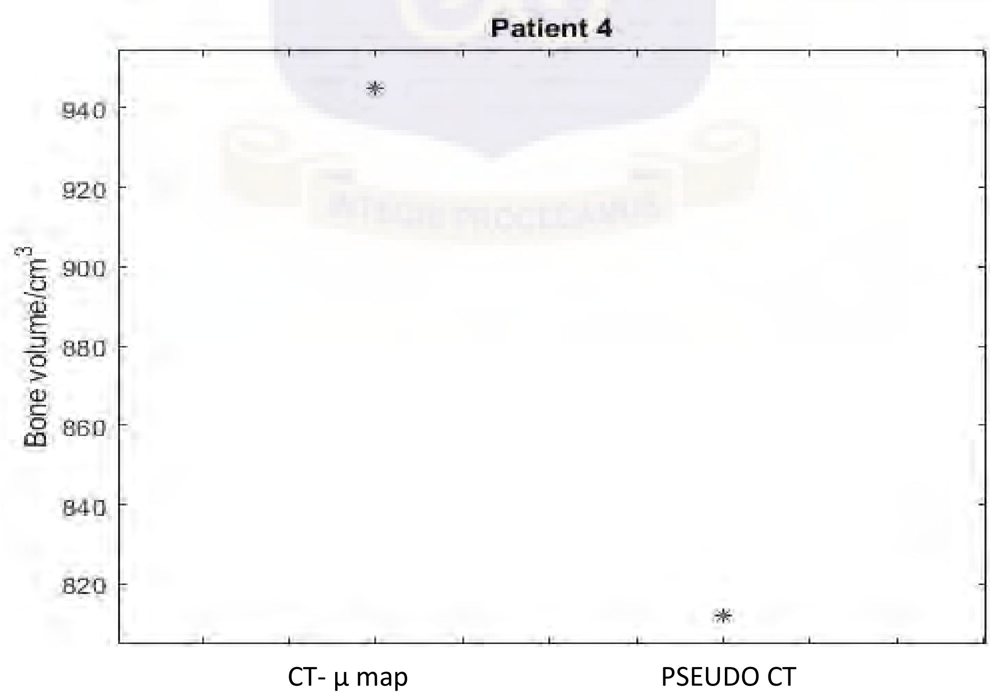

Figure 4.25: Comparison of the bone volume of CT µ-map and pseudo-CT for patient 4.

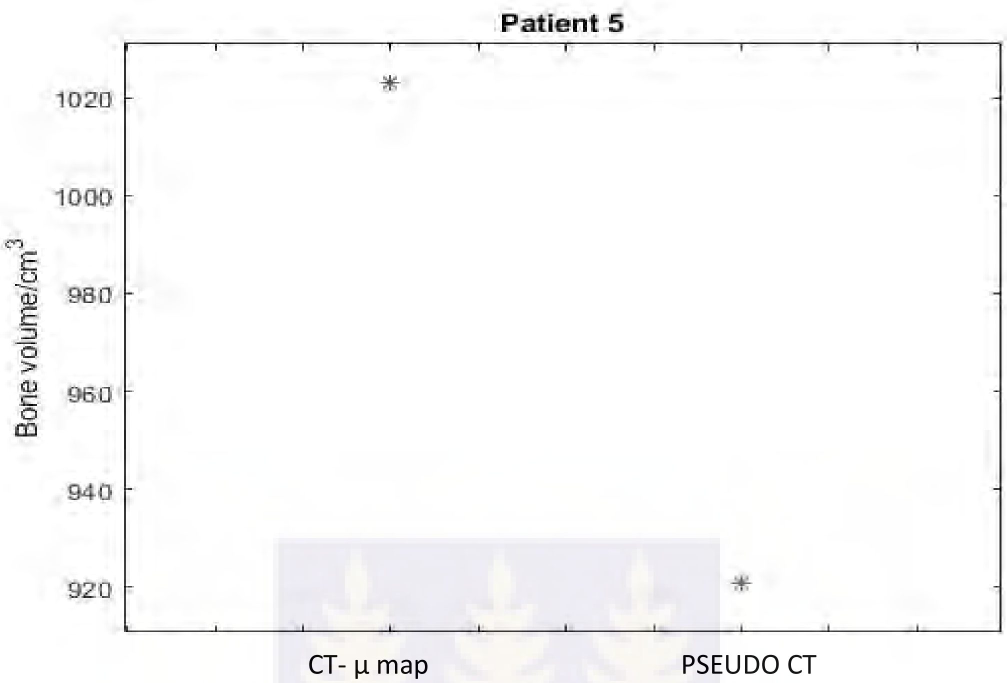

Figure 4.26: Comparison the bone volume of CT µ-map and pseudo-CT for patient 5.

It was observed that the pseudo-CT is not dynamic and there is not much variation in the µ-values. This confirms that the MRI-planner is still a new software and the planners are still working on its development to make it more dynamic and also to generate more consistent µ-values. For all the five images analyzed for the abdominal part of this study, 9000 random µ-values in the bone were ploted. For patient 1, the median µ-values were 0.1725 cm^{-1} and 0.1727 cm^{-1} for CT µ-map and psuedo-CT respectively, finite outliers of 215 and 759 were observed for CT- µ-map and psuedo CT respectively. For patient 2, the median µ-values were 0.1926 cm^{-1} and 0.1690 cm^{-1} for CT- µ-map and psuedo-CT respectively, with finite outliers of 250 and 2 observed for CT- µ-map and psuedo-CT respectively. For patient 3, the median µ-values were 0.1833 cm^{-1} and 0.1737 cm^{-1} for CT- µ-map and psuedo-CT respectively, with finite outliers of 229 and 437 observed for CT-μ-map and psuedo-CT respectively. For patient 4, the median μ-values were 0.1891 cm^{-1} and 0.1712 cm^{-1} for CT- μ-map and psuedo-CT respectively, and finite outliers of 592 and 281 were observed for CT- μ-map and psuedo-CT respectively. For patient 5, the median μ-values were 0.1697 cm^{-1} and 0.1665 cm^{-1} for CT- μ-map and psuedo-CT respectively, finite outliers of 35 and 129 were observed for CT- μ-map and psuedo-CT respectively. From figure 4.27, 4.28, 4.29, 4.30 and 4.31, it was observed that there is much variation in the μ-values, the CT μ-map is more dynamic and has continous values as compared to the pseudo CT which is less dynamic and also μ-values for bone is not continous. Finite outliers of 215 and 759 were observed for CT- μ-map and psuedo-CT respectively.

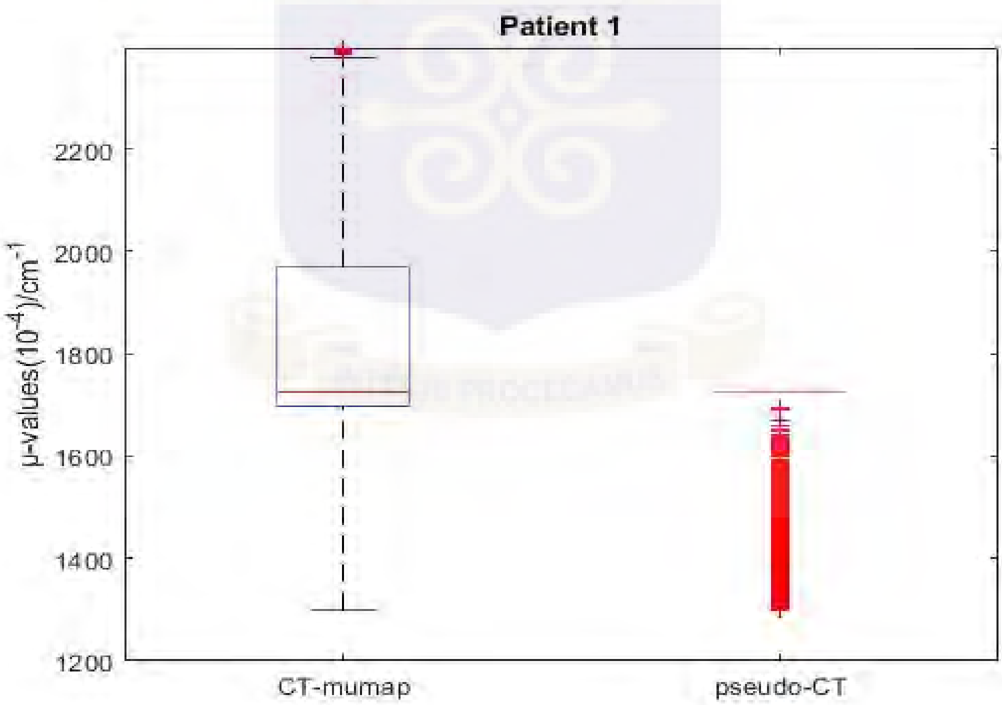

Figure 4.27: Variation in μ-values for bone in CT μ-map and psuedo-CT for patient 1.

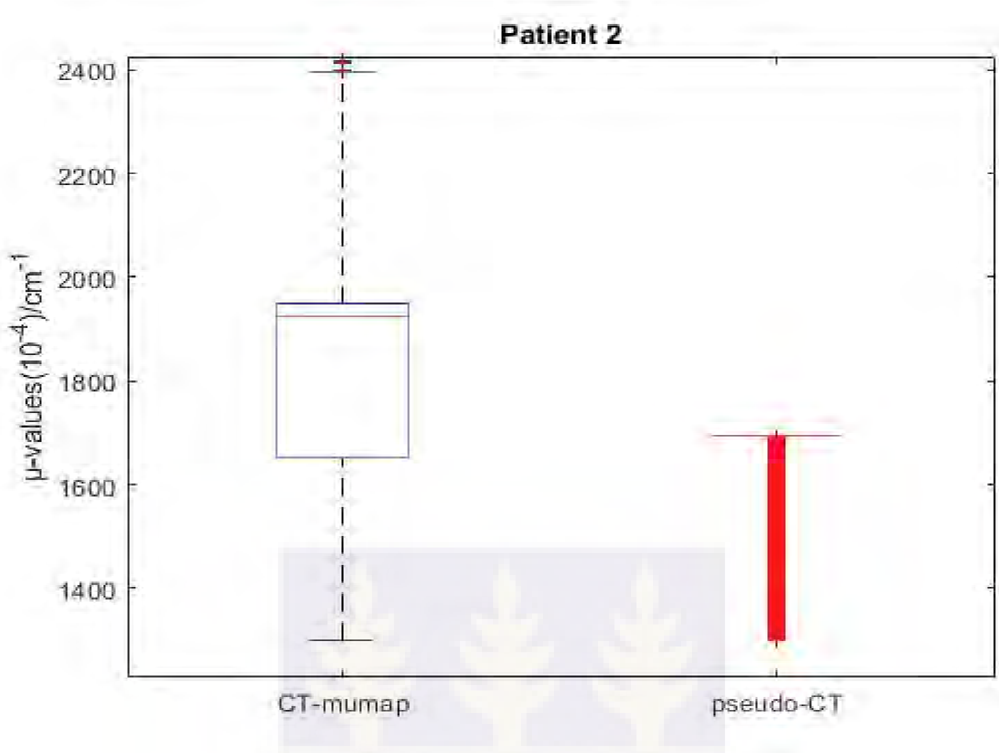

Figure 4.28: Variation in μ-values for bone in CT μ-map and psuedo-CT for patient 2.

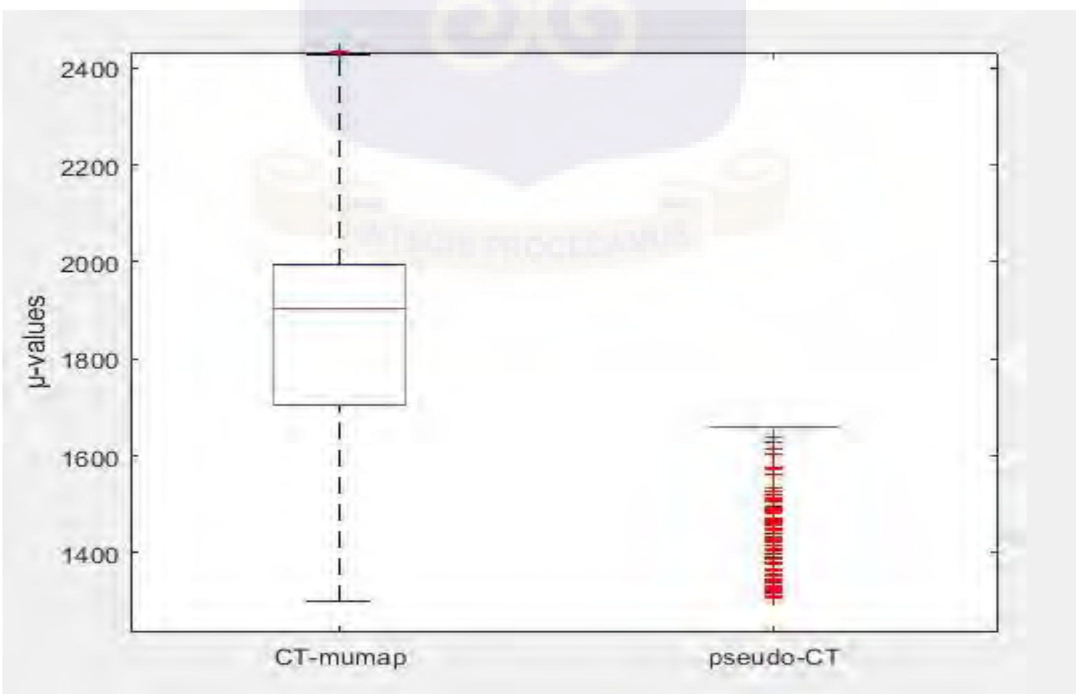

Figure 4.29: Variation in μ-values for bone in CT μ-map and psuedo-CT for patient 3.

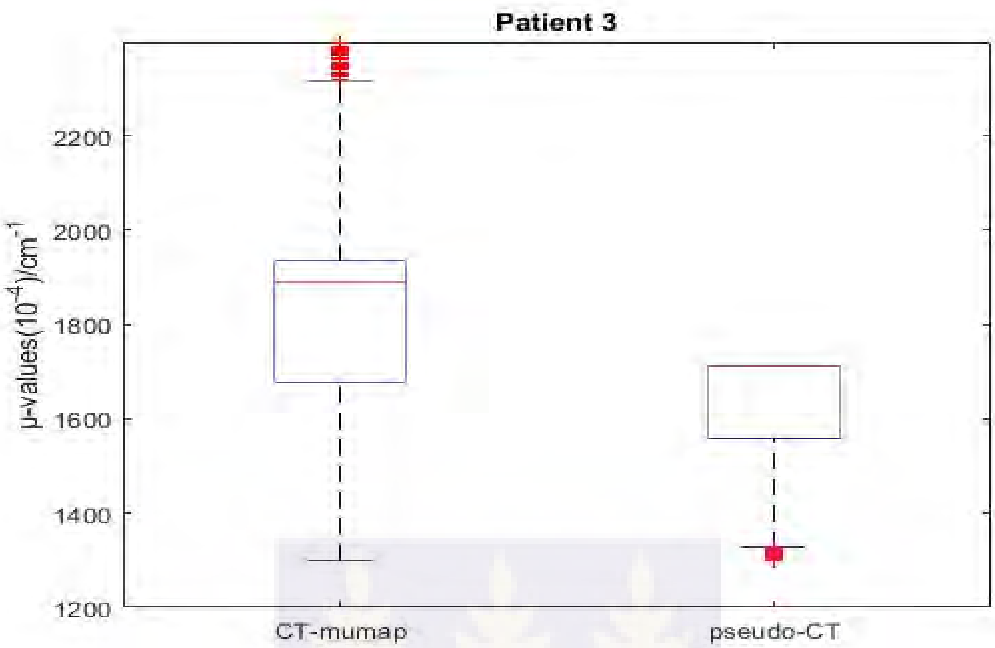

Figure 4.30: Variation in μ-values for bone in CT μ-map and psuedo-CT for patient 4.

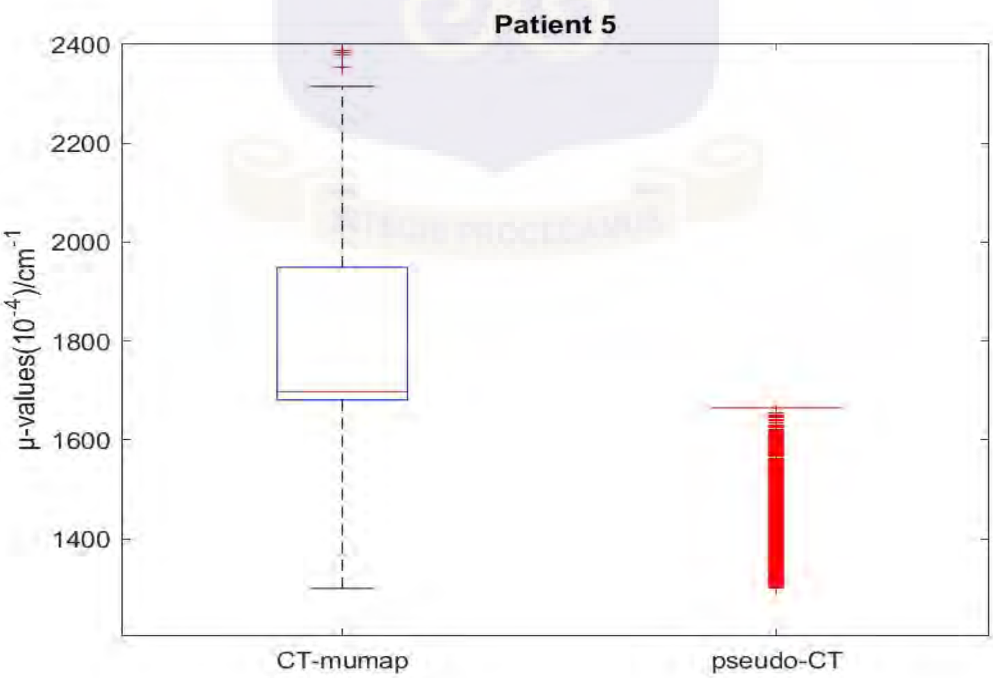

Figure 4.31: Variation in μ-values for bone in CT μ-map and psuedo-CT for patient 5.

4.2.6 Comparison between the CT- μ-Map, MRI- μ-Map and Psuedo CT for Muscle

For patient 1, the mean muscle μ-values were found to be 0.0995 cm^{-1}, 0.0992 cm^{-1} and 0.0995 cm^{-1} for CT- μ-map, Psuedo-CT and MR- μ-map respectively. For all the μ-values plotted, 262, 467 and 376 outliers were found for CT- μ-map, psuedo CT and MR- μ-map respectively as shown in the figure 4.32. For patient 2, the mean muscle μ-values were found to be 0.0989 cm^{-1}, 0.0997 cm^{-1} and 0.0994 cm^{-1} for CT- μ-map, Psuedo-CT and MR- μ-map respectively. For all the μ-values plotted, 425, 487 and 840 outliers were found for CT- μ-map, psuedo-CT and MR- μ-map respectively as shown in the figure 4.33. For patient 3, the mean muscle μ-values were found to be 0.0984 cm^{-1}, 0.0997 cm^{-1} and 0.0988 cm^{-1} for CT- μ-map, psuedo-CT and MR- μ-map respectively. For all the μ-values plotted, 364, 279 and 312 outliers were found for CT μ-map, Psuedo-CT and MR μ-map respectively as shown in the figure 4.34. For patient 4, the mean muscle μ-values were found to be 0.0989 cm^{-1}, 0.0994 cm^{-1} and 0.0995 cm^{-1} for CT μ-map, psuedo CT and MR- μ-map respectively. For all the μ-values plotted 420, 386 and 312 outliers were found for CT μ-map, psuedo-CT and MR μ-map respectively as shown in figure 4.35. For patient 5, the mean muscle μ-values were found to be 0.0986 cm^{-1}, 0.0988 cm^{-1} and 0.0994 cm^{-1} for CT- μ-map, psuedo-CT and MR μ-map respectively. For all the μ-values plotted, 314, 840 and 732 outliers were found for CT μ-map, psuedo-CT and MR μ-map respectively as shown in the figure 4.36. Generally, it was observed that the μ-values for muscle were dynamic for all the μ-maps but was more dynamic and had a greater range in CT μ-map than the Psuedo-CT and MR μ-map.

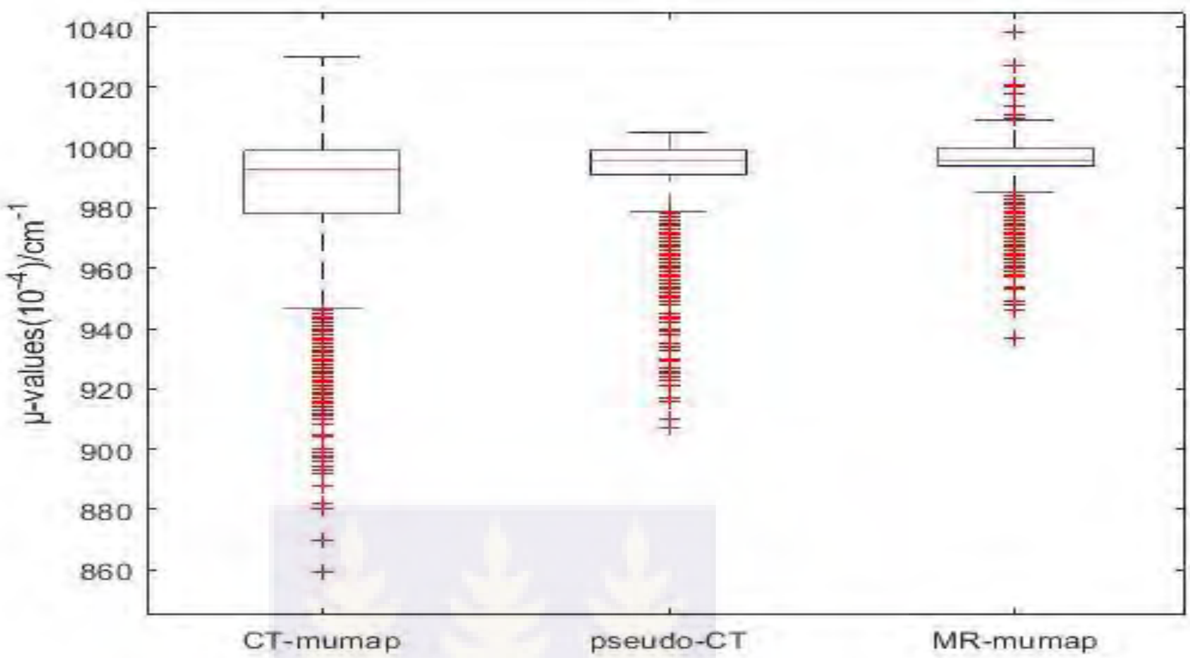

Figure 4.32: Variation in μ-values for muscle in CT- μ-map, psuedo-CT and MR μ-map for patient 1.

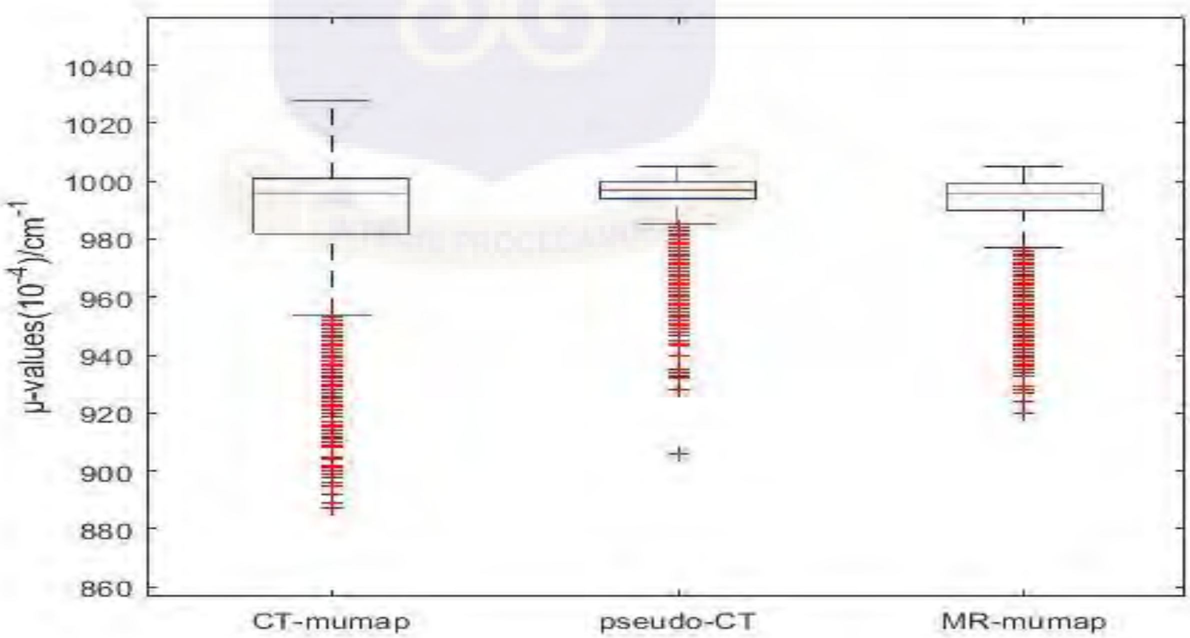

Figure 4.33: Variation in μ-values for muscle in CT- μ-map, psuedo-CT and MR μ-map for patient 2.

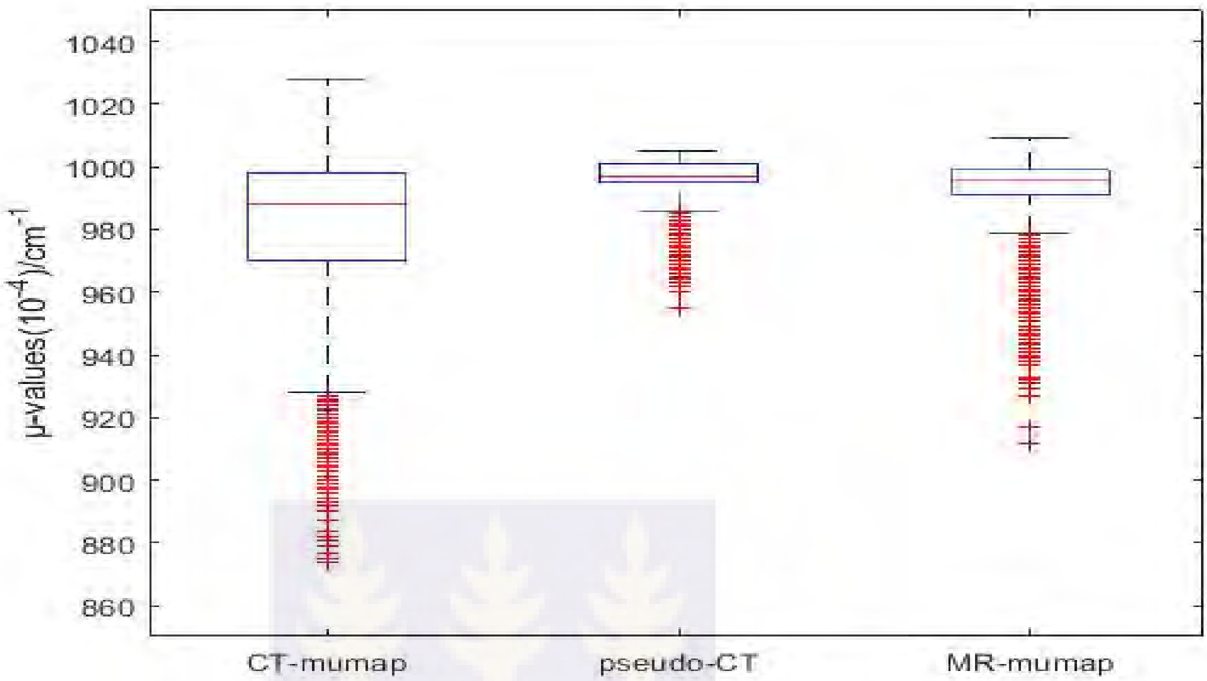

Figure 4.34: Variation in μ-values for muscle in CT- μ-map, psuedo-CT and MR μ-map for patient 3.

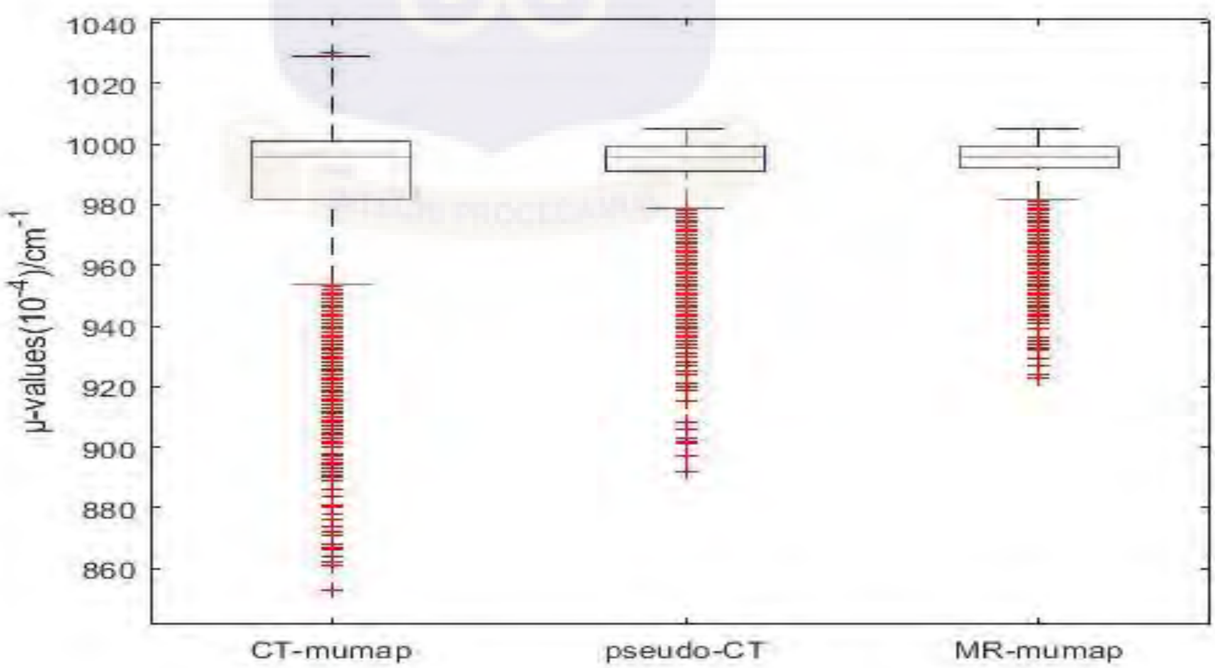

Figure 4.35: Variation in μ-values for muscle in CT- μ-map, psuedo-CT and MR μ-map for patient 4.

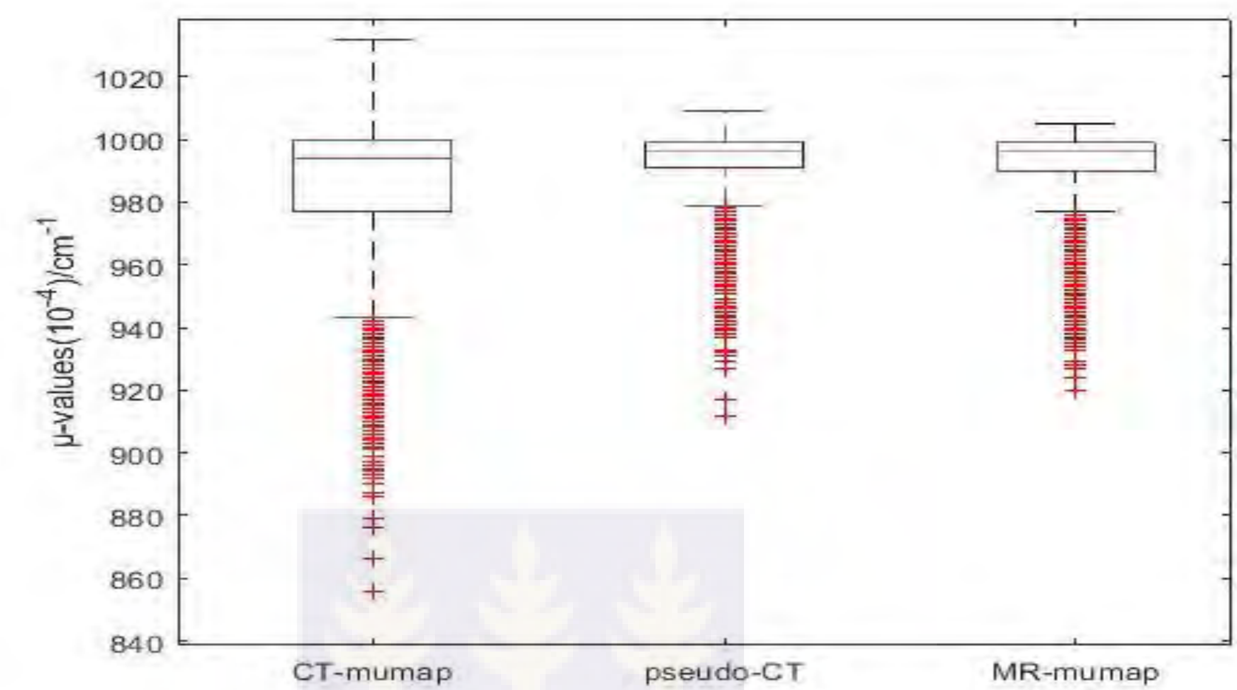

Figure 4.36: Variation in μ-values for muscle in CT- μ-map, psuedo-CT and MR μ-map for patient 5.

CHAPTER FIVE
CONCLUSIONS AND RECOMMENDATION

The chapter presents conclusions and recommendation based on the findings of this research.

5.1 Conclusions

The objective of this study was to compare the similarities and difference in MR-based μ-map and pseudo-CT generation in PET/MR and radiotherapy respectively. MR-based μ-maps were successfully generated and can be used to correct for attenuation in PET, Pseudo-CTs were also successfully generated and can also be used in radiotherapy for dose planning. For head images, it was observed that MR- based μ-maps overestimated the bone as compared to CT μ-map for two patients. For pelvic images, it was found that the pseudo CT underestimated the bone volume in five patients as compared to CT μ-map.

5.2 RECOMMENDATION

It is recommended that further studies should be performed by using pseudo-CT generated from this study for radiotherapy dose planning to analyze how robust the μ-map images are.

REFERENCES

Cabello, J., Lukas, M., Forster, s., Pyka, T., Nekolla, S. G. & Ziegler, S. I. 2015. MR-Based Attenuation Correction Using Ultrashort-Echo-Time Pulse Sequences in Dementia Patients. *J Nucl Med,* 56**,** 423-9.

Carney, J. P., Townsend, D. W., Rappoport, V. & Bendriem, B. 2006. Method for Transforming CT Images for Attenuation Correction In PET/CT Imaging. *Med Phys,* 33**,** 976-83.

Chen, L., Nguyen, T. B., Jones, E., Chen, Z., Luo, W., Wang, L., Price, R. A., Jr., Pollack, A. & Ma, C. M. 2007. Magnetic Resonance-Based Treatment Planning for Prostate Intensity-Modulated Radiotherapy: Creation of Digitally Reconstructed Radiographs. *Int J Radiat Oncol Biol Phys,* 68**,** 903-11.

Chen, Y. & An, H. 2017. Attenuation Correction of PET/MR Imaging. *Magn Reson Imaging Clin N Am,* 25**,** 245-255.

Chin, A., Lin, A. & Anamalayil, S. 2014. Feasibility and Limitations of Bulk Density Assignment in MRI for Head And Neck IMRT Treatment Planning *Med Phys***,** 4851.

Christensen, N. L., Hammer, B. B., Heilt, B. G. & Fetterlyt, K. 1995. Positron Emission Tomography within a Magnetic Field Using Photomultiplier Tubes and Lightguides. Phys. Med. Biol. 691-697.

Commandeur, F., Simon, A., Mathieu, R., Nassef, M., Arango, J. D. O., Rolland, Y., Haigron, P., De Crevoisier, R. & Acosta, O. 2017. MRI to CT Prostate Registration for Improved Targeting in Cancer External Beam Radiotherapy. *IEEE J Biomed Health Inform,* 21**,** 1015-1026.

Dowling, J. A., Lambert, J., Parker, J., Salvado, O., Fripp, J., Capp, A., Wratten, C., Denham, J. W. & Greer, P. B. 2012. An Atlas-Based Electron Density Mapping Method for Magnetic Resonance Imaging (MRI)-Alone Treatment Planning and Adaptive MRI-Based Prostate Radiation Therapy. *Int J Radiat Oncol Biol Phys,* 83**,** E5-11.

Dowling, J. A., Sun, J., Pichler, P., Rivest-Henault, D., Ghose, S., Richardson, H., Wratten, C., Martin, J., Arm, J., Best, L., Chandra, S. S., Fripp, J., Menk, F. W. & Greer, P. B. 2015. Automatic Substitute Computed Tomography Generation and Contouring for Magnetic Resonance Imaging (MRI)-Alone External Beam Radiation Therapy from Standard MRI Sequences. *Int J Radiat Oncol Biol Phys,* 93**,** 1144-53.

Edmund, J. M. & Nyholm, T. 2017. A Review of Substitute CT Generation for MRI-Only Radiation Therapy. *Radiat Oncol,* 12**,** 28.

Eilertsen, K., Vestad, L. N., Geier, O. & Skretting, A. 2008. A Simulation of MRI-Based Dose Calculations on the Basis of Radiotherapy Planning CT Images. *Acta Oncol,* 47**,** 1294-302.

Fuchs, J., Neuberger, T., Rolletschek, H., Schiebold, S., Nguyen, T. H., Borisjuk, N., Borner, A., Melkus, G., Jakob, P. & Borisjuk, L. 2013. A Noninvasive Platform for Imaging and Quantifying Oil Storage in Submillimeter Tobacco Seed. *Plant Physiol,* 161**,** 583-93.

Glide-Hurst, C. K., Low, D. A. & Orton, C. G. 2014. Point/Counterpoint. MRI/CT is the Future of Radiotherapy Treatment Planning. *Med Phys,* 41**,** 110601.

Hofmann, M., Steinke, F., Scheel, V., Charpiat, G., Farquhar, J., Aschoff, P., Brady, M., Scholkopf, B. & Pichler, B. J. 2008. MRI-Based Attenuation Correction for

PET/MRI: a Novel Approach Combining Pattern Recognition and Atlas Registration. *J Nucl Med,* 49**,** 1875-83.

Johansson, A., Karlsson, M., Yu, J., Asklund, T. & Nyholm, T. 2012. Voxel-Wise Uncertainty in CT Substitute Derived From MRI. *Med Phys,* 39**,** 3283-3290.

Johnstone, E., Wyatt, J. J., Henry, A. M., Short, S. C., Sebag-Montefiore, D., Murray, L., Kelly, C. G., Mccallum, H. M. & Speight, R. 2018. Systematic Review of Synthetic Computed Tomography Generation Methodologies for use in Magnetic Resonance Imaging-Only Radiation Therapy. *Int J Radiat Oncol Biol Phys,* 100**,** 199-217.

Jung, J. H., Choi, Y. & Im, K. C. 2016. PET/MRI: Technical Challenges and Recent Advances. *Nucl Med Mol Imaging,* 50**,** 3-12.

Kapanen, M. & Tenhunen, M. 2013. T_1/T_2*-Weighted MRI Provides Clinically Relevant Pseudo-CT Density Data for the Pelvic Bones in MRI-only-Based Radiotherapy Treatment Planning. *Octa Oncol***,** 612-618.

Karlsson, M., Karlsson, M. G., Nyholm, T., Amies, C. & Zackrisson, B. 2009. Dedicated Magnetic Resonance Imaging in the Radiotherapy Clinic. *Int J Radiat Oncol Biol Phys,* 74**,** 644-51.

Keereman, V., Mollet, P., Berker, Y., Schulz, V. & Vandenberghe, S. 2013. Challenges and Current Methods for Attenuation Correction In PET/MRI. *Magma,* 26**,** 81-98.

Paulus, D. H., Quick, H. H., Geppert, C., Fenchel, M., Zhan, Y., Hermosillo, G., Faul, D., Boada, F., Friedman, K. P. & Koesters, T. 2015. Whole-Body PET/MRI Imaging: Quantitative Evaluation of a Novel Model-Based MR Attenuation Correction Method Including Bone. *J Nucl Med,* 56**,** 1061-6.

Peng, B. J., Walton, J. H., Cherry, S. R. & Willig-Onwuachi, J. 2010. Studies of The Interactions of an MRI System With The Shielding In A Combined PET/MRI Scanner. *Phys Med Biol,* 55**,** 265-80.

Peng, B. J., Wu, Y., Cherry, S. R. & Walton, J. H. 2014. New Shielding Configurations For A Simultaneous PET/MRI Scanner at 7t. *J Magn Reson,* 239**,** 50-6.

Pichler, B. J., Judenhofer, M. S. & Wehrl, H. F. 2008. PET/MRI Hybrid Imaging: Devices and Initial Results. *Eur Radiol,* 18**,** 1077-86.

Puttick, S., Bell, C., Dowson, N., Rose, S. & Fay, M. 2015. PET, MRI, and Simultaneous PET/MRI In The Development of Diagnostic and Therapeutic Strategies for Glioma. *Drug Discov Today,* 20**,** 306-17.

Ramsey, C. R. & Oliver, A. L. 1998. Magnetic Resonance Imaging Based Digitally Reconstructed Radiographs, Virtual Simulation, and Three-Dimensional Treatment Planning for Brain Neoplasms. *Med Phys,* 25**,** 1928-34.

Riola-Parada, C., García-Cañamaque, L., Pérez-Dueñas, V., Garcerant-Tafur, M. & Carreras-Delgado, J. L. 2016. Simultaneous PET/MRI versus. PET/CT In Oncology. A Systematic Review. *Revista Española De Medicina Nuclear E Imagen Molecular (English Edition),* 35**,** 306-312.

Shandiz, M. S., Rad, H. S., Ghafarian, P., Karam, M. B., Akbarzadeh, A. & Ay, M. R. 2017. MR-Guided Attenuation Map For Prostate Pet-Mri: An Intensity And Morphologic-Based Segmentation Approach for Generating a Five-Class Attenuation Map in Pelvic Region. *Ann Nucl Med,* 31**,** 29-39.

Siversson, C., Nordstrom, F., Nilsson, T., Nyholm, T., Jonsson, J., Gunnlaugsson, A. & Olsson, L. E. 2015. Technical Note: MRI only Prostate Radiotherapy Planning Using The Statistical Decomposition Algorithm. *Med Phys,* 42**,** 6090-7.

Sjolund, J., Forsberg, D., Andersson, M. & Knutsson, H. 2015. Generating Patient Specific Pseudo-CT of The Head From MR Using Atlas-Based Regression. *Phys Med Biol,* 60**,** 825-39.

Slates, R. B., Keyvan, F., Yiping, S., Marsden, P. K. & Cherry, S. R. 1999. A Study Of Artefacts In Simultaneous PET And MR Imaging Using a Prototype MR Compatible PET Scanner. *Phys In Med & Biol,* 44.

Thorwarth, D., Leibfarth, S. & Mönnich, D. 2013. Potential Role of PET/MRI in Radiotherapy Treatment Planning. *Clin And Trans Img,* 1**,** 45-51.

Wagenknecht, G., Kaiser, H. J., Mottaghy, F. M. & Herzog, H. 2013. Mri For Attenuation Correction In Pet: Methods And Challenges. *Magma,* 26**,** 99-113.

White, D. R., Booz, J., Griffith, R. V., Spokas, J. J. & Wilson, I. J. 2016. Report 44. *ICRU,* Os23**,** Np-Np.

Zaidi, H., Montandon, M.-L. & Slosman, D. O. 2003. Magnetic Resonance Imaging-Guided Attenuation And Scatter Corrections In Three-Dimensional Brain Positron Emission Tomography. *Med Phys,* , 30.

APPENDICES

Sample Scripts

APPENDIX A

Mask Creation.m

```
%load actual image
a=load_untouch_nii('ctnsLYMFOM_025-0801-02001-000483.nii');
load('sCT065_511.mat');
im1 =CTu;
 im1= enegLvl;
imviewer(im1)
%load roi
load('mr_roi.mat')
imlmasked = im1;
imlmasked = double(im1).*(roi.roimask);
mrmasked = imlmasked;
%save image
save_untouch_nii(a,'sCTM025_masked.nii')
laod masked image
im3=load_untouch_nii('sCTM025_masked.nii')
```

APPENDIX B

Image Registration.m

```
% load fixed and moving images
% MRI as fixed image
fixedImage = loadImage3d(fullfile('C:\Users\acqua\Desktop\working
data\LYMFOM_028_LYMFOM_028\PELVIS_T2_HASTE_TRA_0006'));
% CT as moving image
movingImage = loadImage3d('C:\Users\acqua\Desktop\working
data\LYMFOM_028_LYMFOM_028\CT_PELVIS_028');
[regImage, regtransforms] = elxRegister_CTMRI_imageSeries(fixedImage,
movingImage);
save(fullfile('D:\ElxRegistrationFiles','ct_2_mri_regtransforms'),'regtransforms');
return
```

APPENDIX C

HU2PETLAC.m

```
%variable parameters when kvp = 120
valHUair = -1000;
scalingFactor = 10^4;

% constants
a = 5*10^-5;
b = 4.71*10^-2;
BP = 47;
sbBP=9.6*10^-5;
%load image
im=load_untouch_nii('sCTLYMFOM_092_P-1001-00001-000001.nii');
% imviewer(im.img)
% CT = im.img;
%load('ct_2_mri_regtransforms.mat');
CT = im.img;
%CTu = HU2PETLAC(CT,valHUair,scalingFactor);
CT = double(CT);
% CTu = zeros(size(CT));
CT(CT < valHUair) = valHUair;
CTu = CT;
% CTu(CT < valHUair) = valHUair;
% below break point
lowIndxs = find(CT <= BP);
lowHUvoxels = CT(lowIndxs);
CTu(lowIndxs) = sbBP .* (lowHUvoxels + abs(valHUair));
% above break point
highiIndxs = find(CT > BP);
HighHUvoxels = CT(highiIndxs);
CTu(highiIndxs) = a.* (HighHUvoxels + abs(valHUair)) + b;
CTu = uint16(scalingFactor * CTu);
% view image
imviewer(CTu)
save('sCT035_511', 'CTu')
```

APPENDIX D

Bone Volume Creation.m

```
%load image
```

```
iminfo =
loadImage3d('C:\Users\acqua\Desktop\PET_CT_124_PET_CT_124\PET_PETCT_HEL
KROPP_(Adult)_20160928_133341_519000\CT_WB_3_0_B31F_0004');
a=load_untouch_nii('sLYMFOM_017-1001-00001-000001.nii');
imviewer(a.img);
a.img = enegLvl;
imviewer(enegLvl);
%assigning the image
CT = double(enegLvl);
%CT = double(enegLvl);
min = 1300;
boneMask = zeros(size(CT));
boneIndxs = CT >= min;
% for range
%bonerangeIndxs = find(CT >= 300 & CT <=500);
boneMask(boneIndxs)=1;
boneVoxels = find(boneMask==1);
inplaneResol = [iminfo.info(1).PixelSpacing];
sliceThickness = iminfo.info(1).SliceThickness;
interSliceGap = iminfo.info(2).SliceLocation - iminfo.info(1).SliceLocation;
boneVolume = (numel(boneVoxels) * inplaneResol(1) *
inplaneResol(2)*(sliceThickness+interSliceGap))/1000;
boneVolumeIntensities = CT(boneVoxels);
meanBoneInt = mean(boneVolumeIntensities);
%load image 2
iminfo2 =
loadImage3d('C:\Users\acqua\Desktop\PET_MR_124_PET_MR_124\PROSJEKT_MED
IASTINUM_20160928_143202_171000\HEAD_MRAC_DIX_ACONLY_IN_UMAP_0
049');
%load('umap_masked.mat')
imviewer(b.img);
%a.img = enegLvl;
%enegLvl = enegLvl.enegLvl;
%imviewer(enegLvl);
%assigning the image
MRmu = double(b.img);
%CT = double(enegLvl);
min = 1300;
boneMask2 = zeros(size(MRmu));
boneIndxs = find(MRmu >= min);
% for range
%bonerangeIndxs = find(CT >= 300 & CT <=500);
boneMask2(boneIndxs)=1;
boneVoxels2 = find(boneMask2==1);
inplaneResol2 = [iminfo2.info(1).PixelSpacing];
sliceThickness2 = iminfo2.info(1).SliceThickness;
```

```
interSliceGap2 = 4.5 %iminfo2.info(2).SliceLocation - iminfo.info(1).SliceLocation;
boneVolume2 = (numel(boneVoxels2) * inplaneResol(1) *
inplaneResol(2)*(sliceThickness2+interSliceGap2))/1000;
boneVolumeIntensities2 = MRmu(boneVoxels2);
meanBoneInt2 = mean(boneVolumeIntensities2);
```

APPENDIX E

Muscle Volume Creation.m

```
% FOR CTMUMAP
load('ctCTMn025_maskedctCTMn025_masked.mat');
imviewer(CTmasked);
CT=double(CTmasked);
muscleVoxels=find(CT);
muscleIntensities = CT(muscleVoxels);%*10^-1;
meanBoneInt = mean(muscleIntensities);

% for psuedo CT
load('sCTM025_masked.mat');
imviewer(imlmasked);
sCT=double(imlmasked);
muscleVoxels2=find(sCT);
muscleIntensities2 = sCT(muscleVoxels2);
meanBoneInt2 = mean(muscleIntensities2);

% FOR MRMUMAP
load('mr_masked.mat');
imviewer(mrmasked);
mr=double(mrmasked);
muscleVoxels3=find(mr);
muscleIntensities3 = mr(muscleVoxels3);
meanBoneInt3 = mean(muscleIntensities3);

% MRmu = load_untouch_nii('sCTLYMFOM_035_I-1001-00001-000001.nii');
% imviewer(MRmu.img);
% MR=double(MRmu.img);
% muscleVoxels3=find(MR);
% muscleIntensities3 = MR(muscleVoxels3);
% meanBoneInt3 = mean(muscleIntensities3);
return
```

APPENDIX F

box plot.m

```
% BOXPLOT
example_ct_boneIntensities = muscleIntensities (1:7875,1);
example_sct_boneIntensities = muscleIntensities2 (1:7875,1);
example_mri_boneIntensities = muscleIntensities3 (1:7875,1)';
figure, boxplot([example_ct_boneIntensities,example_sct_boneIntensities,
example_mri_boneIntensities'], 'Labels',{'CT-mumap','pseudo-CT','MR-mumap'})
ylim([800 1000]);
ylabel('µ-values(10^-^4)/cm^-^1');
```

APPENDIX G

Scatter Plot Script.m

```
load('im130_511.mat')
im130MRT2=load_untouch_nii('sPET_MRT2_130-0049-00001-000003-01.nii');
testCT=rot90(enegLvl,3);
im130MRT2.img= testCT;
save_untouch_nii(im130MRT2,'CT130_coreg_MRT2_49.nii')
imCT=load_untouch_nii('CT130_coreg_MRT2_49.nii');
imMRAC=load_untouch_nii('rsPET_MRmu_124-0049-00001-000001-02.nii');
imMRAC.img = imMRAC.img.*1e-4;
imCT_cor=mean(testCT,2);
imMRAC_cor=mean(imMRAC.img,2);
imviewer(squeeze(imMRAC_cor))
imviewer(squeeze(imCT_cor))
figure,plot(imCT_cor(:),imMRAC_cor(:),'.')
```